Empirical constraints on the turbulence in QSO host nebulae from velocity structure function measurements

Mandy C. Chen [1]★ Hsiao-Wen Chen,[1] Michael Rauch,[2] Zhijie Qu [1] Sean D. Johnson [3]
Jennifer I-Hsiu Li,[3] Joop Schaye [4] Gwen C. Rudie,[2] Fakhri S. Zahedy [2] Erin Boettcher,[5,6,7]
Kathy L. Cooksey[8] and Sebastiano Cantalupo[9]

[1]*Department of Astronomy and Astrophysics, The University of Chicago, Chicago, IL 60637, USA*
[2]*The Observatories of the Carnegie Institution for Science, 813 Santa Barbara Street, Pasadena, CA 91101, USA*
[3]*Department of Astronomy, University of Michigan, Ann Arbor, MI 48109, USA*
[4]*Leiden Observatory, Leiden University, PO Box 9513, NL-2300 RA Leiden, the Netherlands*
[5]*Department of Astronomy, University of Maryland, College Park, MD 20742, USA*
[6]*X-ray Astrophysics Laboratory, NASA/GSFC, Greenbelt, MD 20771, USA*
[7]*Center for Research and Exploration in Space Science and Technology, NASA/GSFC, Greenbelt, MD 20771, USA*
[8]*Department of Physics and Astronomy, University of Hawai'i at Hilo, Hilo, HI 96720, USA*
[9]*Department of Physics, University of Milan Bicocca, Piazza della Scienza 3, I-20126 Milano, Italy*

ABSTRACT

We present the first empirical constraints on the turbulent velocity field of the diffuse circumgalactic medium around four luminous quasi-stellar objects (QSOs) at $z \approx 0.5$–1.1. Spatially extended nebulae of $\approx$50–100 physical kpc in diameter centred on the QSOs are revealed in [O II] $\lambda\lambda$ 3727, 3729 and/or [O III] λ 5008 emission lines in integral field spectroscopic observations obtained using Multi-Unit Spectroscopic Explorer on the Very Large Telescope. We measure the second- and third-order velocity structure functions (VSFs) over a range of scales, from $\lesssim$5 kpc to $\approx$20–50 kpc, to quantify the turbulent energy transfer between different scales in these nebulae. While no constraints on the energy injection and dissipation scales can be obtained from the current data, we show that robust constraints on the power-law slope of the VSFs can be determined after accounting for the effects of atmospheric seeing, spatial smoothing, and large-scale bulk flows. Out of the four QSO nebulae studied, one exhibits VSFs in spectacular agreement with the Kolmogorov law, expected for isotropic, homogeneous, and incompressible turbulent flows. The other three fields exhibit a shallower decline in the VSFs from large to small scales. However, with a limited dynamic range in the spatial scales in seeing-limited data, no constraints can be obtained for the VSF slopes of these three nebulae. For the QSO nebula consistent with the Kolmogorov law, we determine a turbulence energy cascade rate of $\approx$0.2 cm^2 s^{-3}. We discuss the implication of the observed VSFs in the context of QSO feeding and feedback in the circumgalactic medium.

Key words: turbulence – surveys – galaxies: haloes – quasars: general.

1 INTRODUCTION

The tenuous gas residing in the circumgalactic medium (CGM) contains a critical record of the past and ongoing interactions between galaxies and their surrounding environment. Characterizing the detailed physical properties of the CGM is an important step in improving current galaxy evolution models. Over the past three decades, absorption spectroscopy using pre-dominantly quasi-stellar object (QSO) sightlines has yielded sensitive constraints on various properties of the CGM, and provided us with an increasingly intricate picture of the gaseous halo ecosystem (see e.g. Chen 2017; Tumlinson, Peeples & Werk 2017; Rudie et al. 2019; and references therein). Observations have shown that the CGM contains multiphase gas spanning a wide range in density, temperature, ionization state,

and metallicity (e.g. Savage et al. 2005; Zahedy et al. 2019, 2021; Cooper et al. 2021). Numerical simulations have also shown that different dynamical processes, such as gas infall, outflow, and tidal interactions, can also happen in the CGM to drive and regulate galaxy growth over cosmic time (e.g. Anglés-Alcázar et al. 2017; van de Voort 2017; Mitchell & Schaye 2022).

However, the lack of spatial information from the 'pencil-beam' probe of absorption spectroscopy has hindered our ability to robustly characterize the thermodynamic state of the gas. While the Doppler width of absorption profiles exceeding the value of thermal broadening may provide evidence for the presence of non-thermal pressure support in the CGM (e.g. Rauch et al. 1996; Rudie et al. 2019), interpretations of the physical origin of the non-thermal motions remain ambiguous because both large-scale coherent flows and turbulent motions contribute to the observed line broadening. Similar ambiguities exist in kinematic studies of emission signals obtained through long-slit or single-aperture spectroscopy.
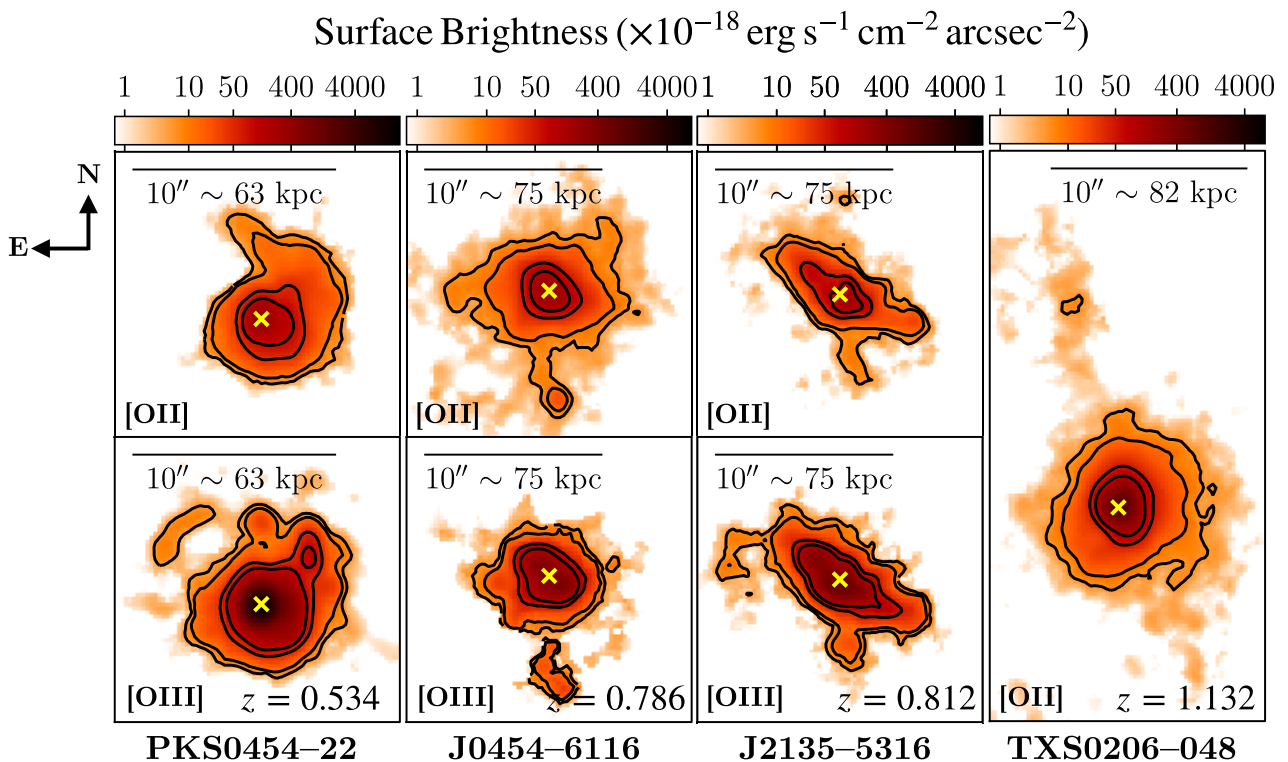
★ E-mail: mandychen@uchicago.edu

Surface Brightness ($\times 10^{-18}$ erg s^{-1} cm^{-2} arcsec^{-2})

Figure 1. Continuum- and QSO-subtracted narrow-band images of the [O II] and [O III] emission from the four fields studied in this paper, based on the MUSE-WFM observations. The fields are shown in the order of increasing redshift from left to right. For TXS0206−048, the [O III] line is redshifted out of the MUSE wavelength coverage and is therefore not shown here. Contours are at surface brightness levels of $[5, 10, 50, 100] \times 10^{-18}$ erg s^{-1} cm^{-2} arcsec^{-2}. The yellow cross in each panel marks the quasar position.

Diffuse, ionized plasmas such as the CGM are expected to be turbulent, because of the expected high Reynolds number (see Burkhart 2021 for a recent review). The presence of turbulence in the diffuse halo gas and the degree of such turbulence have profound implications for the thermal and dynamic properties of the CGM. Turbulent energy can be a significant source of heating to offset cooling in the hot halo through non-linear interactions between large and small eddies (e.g. McNamara & Nulsen 2007; Zhuravleva et al. 2014). In addition, turbulence produces density fluctuations, triggering and facilitating multiphase condensation in the hot halo (e.g. Gaspari et al. 2018; Fielding et al. 2020; Gronke et al. 2022). Turbulent mixing also provides an efficient transport mechanism for metals from star-forming regions to the CGM/IGM, and can facilitate the mixing of metals within the CGM (e.g. Pan & Scannapieco 2010). Given these vital scientific implications, it is of great interest to obtain direct empirical constraints on turbulence in the CGM.

In this context, the recent advent of high-throughput, wide-field integral field spectrographs (IFSs) such as the Multi-Unit Spectroscopic Explorer (MUSE; Bacon et al. 2010) on the Very Large Telescope (VLT) has transformed CGM investigations by providing two-dimensional contiguous maps of large-scale line-emitting signals with unprecedented sensitivities and efficiency. Compared with absorption spectroscopy, the spatial information provided by these IFS data reveals new insights into the detailed physical processes of these low-density regions. In particular, spatially resolved kinematic properties now enable two-point statistical measurements of the velocity field, providing an exciting opportunity to probe turbulence beyond a single sightline/aperture approach.

One of the standard two-point probes is the velocity structure function (VSF), defined as

$$S_p(r) = \langle |\boldsymbol{v}(\boldsymbol{x}) - \boldsymbol{v}(\boldsymbol{x} + \boldsymbol{r})|^p \rangle, \tag{1}$$

where $\boldsymbol{x}$ and $\boldsymbol{r}$ represent, respectively, the spatial location of a starting point and the distance between the starting point and a second location for calculating the pair velocity difference (e.g. Frisch 1995). Different variants of the VSFs record the mean pair velocity difference to the power of p averaged over all available pair configurations for a given separation $r \equiv |\boldsymbol{r}|$. There have been extensive efforts, both in observations and numerical simulations, in using VSFs to probe the thermodynamic state of the interstellar medium (ISM) in local H II regions and in molecular clouds (e.g. Wen & O'dell 1993; Ossenkopf & Mac Low 2002; Federrath 2013; Arthur, Medina & Henney 2016; Padoan et al. 2016; Anorve-Zeferino 2019; Chira et al. 2019; Melnick, Tenorio-Tagle & Telles 2021; Hu et al. 2022). Recently, VSFs have also been measured for Milky Way stars using *GAIA* data (Ha et al. 2021, 2022). These studies in the local Universe have shown that not only is turbulence ubiquitous in the ISM, but it also plays a critical role in shaping the star formation processes inside a galaxy (see e.g. Burkhart 2021 for a review).

For the CGM, measuring VSFs becomes more challenging because of faint emission signals and because of a lack of two-dimensional velocity maps with sufficiently fine spatial sampling, particularly for sources beyond the local Universe where cosmological surface brightness dimming further weakens the signal strength. Rauch, Sargent & Barlow (2001) attempted the first second-order VSF measurements in the low-density circum- and intergalactic gas at redshift $z \approx 2-3$, using C IV absorbers identified along multiply-

Table 1. Summery of the QSO properties.

Field name	Redshift	N_{group}^a	$\sigma_{v,\text{group}}^b$ (km s^{-1})	Radio mode
PKS0454−22^c	0.5335	23	≈320	Loud
J0454−6116^d	0.7861	18	≈300	Quiet
J2135−5316	0.8115	2	–	Quiet
TXS0206−048^e	1.1317	27	≈550	Loud

^{a}Number of spectroscopically identified group member galaxies.
^{b}Velocity dispersion of the group.
^{c}QSO properties of PKS0454−22 are adopted from Helton et al. (2021). While the authors identified 23 galaxies with $|\Delta v| < 1500$ km s^{-1} and $d \lesssim 300$ kpc from the QSO location, the velocity distribution of these galaxies is clearly asymmetric with a tail extending to ≈1500 km s^{-1}. The velocity dispersion referenced here is calculated using 19 galaxies with $|\Delta v| < 1000$ km s^{-1}.
^{d}For both J0454−6116 and J2135−5316, group member galaxies are found with $|\Delta v| < 1000$ km s^{-1} from the QSO redshift and $d \lesssim 250$ kpc from the QSO location (J. Li private communication).
^{e}For TXS0206−048, group member galaxies are found with $|\Delta v| < 1500$ km s^{-1} from the QSO redshift and $d \lesssim 500$ kpc from the QSO location (Johnson et al. 2022).

lensed QSO sightlines. The VSFs in Rauch et al. (2001) were found to be consistent with expectations from the Kolmogorov turbulence (Kolmogorov 1941, also see the discussion below in Section 2), but the uncertainties were large and the spatial sampling was sparse. Recently, Li et al. (2020) measured the first-order VSF using Hα filaments detected in IFS data near the centers of nearby cool core clusters. These authors identified a bump in the VSFs at 20–30 kpc, which they attributed to energy injections by rising bubbles powered by the supermassive black holes at the centers of these galaxy clusters. Studies such as these demonstrate that measuring the VSF provides a promising tracer of energy coupling and cascades from the source at the galactic center to the diffuse gas reservoir on 10–30 kpc scales.

Motivated by Li et al. (2020), we have carried out a detailed analysis of the velocity field observed in four QSO-host nebulae. These nebulae are revealed by extended emission (up to a scale of ∼100 physical kpc in diameter) in [O II] $\lambda\lambda$ 3727, 3729 and/or [O III] λ 5008 lines (see Fig. 1). These four fields span a range in redshift from $z_{\text{QSO}} \approx 0.5$ to $z_{\text{QSO}} \approx 1.1$, constituting the first $z \gtrsim 0.5$ sample with two-point characterizations of the CGM velocity field. While all fields host a bright QSO with a bolometric luminosity of ∼10^{47} erg s^{-1}, these QSOs span a range in radio luminosity and reside in diverse group environments with different numbers of neighbouring galaxies found (see Table 1 for a summary of the QSO properties). We have measured the second- and third-order VSFs over a range of scales, from $\lesssim 5$ kpc to ≈20–50 kpc in these nebulae. While no constraints on the energy injection and dissipation scales can be obtained from the current data, we are able to determine a robust power-law slope after accounting for the effects of atmospheric seeing, spatial smoothing, and large-scale bulk flows. This work represents the first empirical study to resolve the turbulent velocity field in the CGM beyond the nearby Universe.

This paper is organized as follows. First, we illustrate the basic formalism of VSFs in Section 2, and discuss how the smoothing and projection effects in observational data can affect the VSF measurement. In Section 3, we present the IFS data used in this work, the subsequent emission-line analyses, as well as the VSF measurements. The results are presented in Section 4. We discuss our results in Section 5, and conclude in Section 6. Throughout this paper, we adopt a Hubble constant of $H_0 = 70$ km s^{-1} Mpc^{-1}, $\Omega_M = 0.3$,

and $\Omega_\Lambda = 0.7$ when deriving distances, masses, and luminosities. All distances quoted are in physical units.

2 VELOCITY STRUCTURE FUNCTIONS AS A TRACER OF TURBULENCE

As defined in equation (1), the VSF quantifies the kinetic energy fluctuations as a function of scale in a velocity field. Kolmogorov (1941) showed that for isotropic, homogeneous, and incompressible flows with sufficiently large Reynolds numbers, the VSF should follow a power-law scaling of $S_p(r) \propto r^{p/3}$. In particular, the second-order VSF $S_2(r) \propto r^{2/3}$ is directly related to the autocorrelation function $\Gamma(r)$ and the kinetic energy power spectrum E_k of an isotropic velocity field through

$$S_2(r) = 2[\Gamma(0) - \Gamma(r)] = 2 \int (1 - e^{ikr}) E_k \, dk, \qquad (2)$$

where

$$\Gamma(r) = \langle \boldsymbol{v}(\boldsymbol{x})\boldsymbol{v}(\boldsymbol{x} + \boldsymbol{r}) \rangle \qquad (3)$$

and $k = 2\pi/r$. The energy power spectrum then scales with k following $E_k \propto k^{-5/3}$. Similarly, the third-order VSF $S_3(r) \propto r$ can be derived exactly to follow $S_3(r) = -(4/5) \epsilon r$, where ϵ represents the energy cascade rate (also see Section 5.1 for a discussion on ϵ).

While these theoretical expectations of VSFs are established in three-dimensional space, empirical data are limited to projected quantities. Specifically, the velocity differences are measured along the line of sight based on the observed Doppler shifts, and only projected separations r_{proj} along the plane of the sky are accessible instead of the true three-dimensional distances between two locations. Such limitations need to be accounted for explicitly when interpreting observational results.

The effect of projections in the observed VSFs has been investigated extensively by previous authors. When viewing a cloud with well-established three-dimensional Kolmogorov turbulence in projection, von Hoerner (1951) demonstrated that the shape of the measured VSF depends on the depth, L, of the cloud along the line of sight. At separations $r_{\text{proj}} < L$, the VSF is expected to steepen, with a power-law slope of $5p/6$, but it recovers to the theoretical value of $p/3$ at larger separations $r_{\text{proj}} > L$. There is a smooth transition between the two regimes that could be used as a probe of the cloud depth L (von Hoerner 1951). This effect, sometimes referred to as 'projection smoothing,' is also verified by several other studies both analytically (e.g. O'dell & Castaneda 1987; Xu 2020) and in numerical simulations (e.g. Mohapatra et al. 2022). Meanwhile, a recent study by Zhang et al. (2022) suggests that if the emission source is more spatially confined (e.g. Hα filaments at the center of some galaxy clusters), the projection effect will flatten the VSF as opposed to making it steeper.

In addition to line-of-sight projection effects, the spatial correlation due to atmospheric seeing in ground-based data will also alter the shape of the measured VSF. Additional spatial smoothing often applied to enhance the signal-to-noise ratio (SNR) of noisy data would further increase the scale of the spatially correlated signal. Fortunately, this effect can be analytically incorporated into the theoretical models of the second-order VSF S_2, allowing a more accurate comparison between data and model expectations. Based on equation (2), the second-order VSF of a spatially smoothed velocity field can be written as

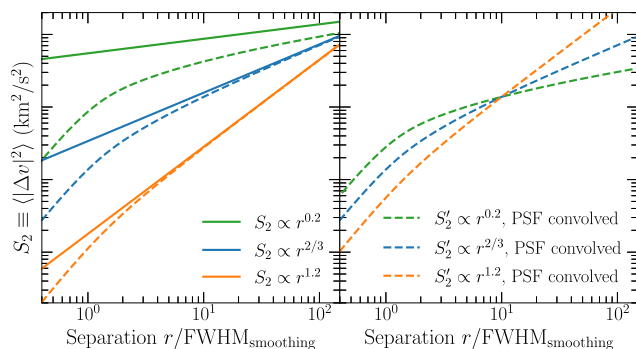$$S_2'(r) = 2[\Gamma'(0) - \Gamma'(r)]. \qquad (4)$$

Figure 2. *Left*: Illustration of the spatial smoothing effect on the shape of the second-order VSF. Green, blue, and orange solid lines show power-law $S_2(r)$ with an intrinsic slope of $\gamma_2 = 0.2$, 2/3 (i.e. Kolmogorov slope), and 1.2, respectively. The corresponding dashed curves show the shapes of $S_2'(r)$ after convolving with a Gaussian smoothing kernel, calculated with equations (4)–(7). It can be seen that spatial smoothing significantly steepens the VSF at $r \lesssim 2 \times \mathrm{FWHM}_{\mathrm{smoothing}}$, and the discrepancy is stronger for a flatter intrinsic VSF, as discussed in the text. *Right*: Smoothed $S_2'(r)$ curves, same as shown in the left column, re-normalized to the same value at $r = 10 \times \mathrm{FWHM}_{\mathrm{smoothing}}$. This panel shows that with an accurate estimate of the smoothing kernel size, the intrinsic VSF slope can be obtained with high-SNR measurements even if the probed spatial scale does not cover a large dynamic range.

$\Gamma'(r)$ is the autocorrelation function of the smoothed velocity field and can be calculated by

$$\Gamma'(r) = \langle \boldsymbol{v}'(\boldsymbol{x})\boldsymbol{v}'(\boldsymbol{x} + \boldsymbol{r}) \rangle = \boldsymbol{v}' \otimes \boldsymbol{v}', \tag{5}$$

where $\boldsymbol{v}'$ is the smoothed velocity field. If we designate $\boldsymbol{g}(\boldsymbol{x})$ as the spatial smoothing kernel, then the smoothed velocity field can be expressed as convolution of $\boldsymbol{v}$ with a Gaussian kernel representing the total point spread function (PSF), $\boldsymbol{v}'(\boldsymbol{x}) = \boldsymbol{g}(\boldsymbol{x}) * \boldsymbol{v}(\boldsymbol{x})$. Equation (5) can now be rewritten as

$$\Gamma'(r) = \boldsymbol{v}' \otimes \boldsymbol{v}' = (\boldsymbol{g} * \boldsymbol{v}) \otimes (\boldsymbol{g} * \boldsymbol{v}). \tag{6}$$

Equation (6) can be rearranged to a simple analytic form of

$$\Gamma'(r) = (\boldsymbol{g} \otimes \boldsymbol{g}) * (\boldsymbol{v} \otimes \boldsymbol{v}) = \Gamma_g(r) * \Gamma(r). \tag{7}$$

Equation (7) shows that the autocorrelation function of a smoothed velocity field can be calculated through a convolution of two functions: the autocorrelation function of the smoothing kernel and the autocorrelation function of the intrinsic, unsmoothed velocity field. When both $\Gamma_g(r)$ and $\Gamma(r)$ have analytical expressions, such as the case for a Gaussian smoothing kernel and a power-law autocorrelation function, $\Gamma'(r)$ can be calculated explicitly and an exact expression for S_2' can be obtained through equation (4).

To visualize this spatial smoothing effect, we perform a series of calculations, adopting three different intrinsic power-law slopes for S_2, corresponding to a relatively flat VSF with a slope of $\gamma_2 = 0.2$, a Kolmogorov VSF of $\gamma_2 = 2/3$, and a steeper VSF of $\gamma_2 = 1.2$. Assuming a Gaussian kernel for spatial smoothing, the comparisons of the intrinsic S_2 and the smoothed S_2' are shown in Fig. 2. It is clear that the smoothing effect is more significant for a flatter intrinsic VSF. This can be understood intuitively by noting that a flatter VSF carries significantly more relative power on small scales, corresponding to large k modes. As a result, spatial smoothing, which by design removes the power from large k modes, will have a more significant impact in systems with a flatter energy power spectrum. Taking the Kolmogorov VSF for reference, Fig. 2 shows that the measured VSF begins to recover the intrinsic, unsmoothed VSF at separations $\gtrsim 4$ times the full width at half-maximum (FWHM) of the smoothing

kernel. We, therefore, emphasize the importance of explicitly taking into account this smoothing effect in VSF measurements, especially when working with data where the seeing size is relatively large compared with the scales probed.

For the QSO nebulae included in the current study, the spatial scales probed are restricted to $\lesssim 10$ times the FWHM of the PSF (see Section 3). Fortunately, as we show in the right-hand panel of Fig. 2, with sufficient SNR in the VSF measurements and an accurate estimate of the PSF size, the intrinsic VSF slope can still be recovered even when working with a limited dynamic range. Similarly, for the VSF measurements of H α filaments in cluster cores (Li et al. 2020), the steeper slopes may be partially attributed to the spatial smoothing effect due to the limited dynamic range compared to the size of the seeing disc in the data.

We have demonstrated that it is straightforward to incorporate any spatial smoothing present in the data to the second-order VSF measurements, thanks to the convenient relation between S_2 and the autocorrelation function $\Gamma(r)$. It is less straightforward to do so for the third-order VSFs, from which we expect to infer the energy cascade rate based on the exact relation of $S_3(r) \propto \epsilon r$ (see the discussion in Section 5.1). Benzi et al. (1993) reported the existence of an extended self-similarity (ESS), where VSFs of different orders are tightly correlated with each other and roughly following a simple power-law function. The ESS is useful because it applies to cases with both high and low Reynolds numbers. For example, for cases with low Reynolds numbers, the second-order VSFs may not follow the expected power-law scaling relation due to a lack of a well-established inertial range. However, with ESS, the third-order VSFs can still be inferred to constrain the energy cascade rate. In addition, with a simulated velocity field generated using Fourier series (see e.g. Saad et al. 2017), we have tested that the spatial smoothing effect does not alter the power-law scaling relation for ESS. In other words, if a velocity field exhibits an ESS relation of $S_p = \alpha S_3^{\gamma_p/\gamma_3}$, then this scaling relation is preserved as $S_p' = \alpha S_3'^{\gamma_p/\gamma_3}$ after the velocity field is smoothed. In Sections 4.1 and 5.3 below, we show that the ESS is observed in all systems and discuss the caveats associated with this observation.

3 OBSERVATIONS AND MEASUREMENTS

To measure the VSFs in extended nebulae, spatially resolved velocity maps are necessary. In this section, we described the wide-field IFS observations available for detecting extended nebulae around four QSO hosts and the constructions of velocity maps based on line profile analyses of [O II] $\lambda\lambda$ 3727, 3729 and [O III] λ 5008 emission lines.

3.1 IFS observations

Wide-field IFS data of the QSO fields were obtained using the Multi-Unit Spectroscopic Explorer (MUSE; Bacon et al. 2010) on the VLT UT4. All four fields were observed under the Wide-Field-Mode (WFM), which provides a contiguous field of view (FOV) of 1 arcmin × 1 arcmin in a single pointing, with 0.2 arcsec per pixel spatial sampling. MUSE covers a wavelength range of 4750–9350 Å with a resolving power of $R \approx 2000$–4000 (higher at the longer wavelength end).

Out of the four fields, J0454−6116 and J2135−5316 were obtained as part of the Cosmic Ultraviolet Baryon Survey (CUBS) using adaptive optics assisted WFM under program ID, 0104.A-0147 (PI: H.-W. Chen; Chen et al. 2020). The total exposure time was

Table 2. Journal of MUSE observations.

Field name	RA(J2000)	Dec.(J2000)	t_{exp} (s)	Seeing[a] (arcsec)
PKS0454−22	04:56:08.90	−21:59.09.1	2700	0.6
J0454−6116	04:54:15.95	−61:16:26.6	5100	0.7
J2135−5316	21:35:53.20	−53:16:55.8	6840	0.6
TXS0206−048	02:09:30.74	−04:38:26.5	28800	0.7

[a]Atmospheric seeing FWHM measured using the QSO at 7000 Å. To improve the quality of line fitting, each combined data cube was convolved with a Gaussian kernel of FWHM = 0.7 arcsec. This yielded a total PSF FWHM of ≈0.9–1.0 arcsec (see Section 3.3), corresponding to a projected separation of 6–8 kpc at the redshifts of these QSOs.

5100s for J0454−6116 and 6840s for J2135−5316. PKS0454−22 was observed under program ID 0100.A-0753 (PI: C. Péroux; Péroux et al. 2019), with a total exposure time of 2700s. TXS0206−048 was part of the MUSE Quasar-field Blind Emitters Survey (MUSE-QuBES) under program IDs 097.A-0089(A) and 094.A-0131(B) (PI: J. Schaye; Muzahid et al. 2020) with a total exposure time of 28 800s. All observations were carried out under good seeing conditions, with the mean seeing FWHM measured to be ≈0.6–0.7 arcsec at the location of the QSOs at 7000 Å. A summary of the MUSE observations, including the mean seeing in the final combined data cube, is listed in Table 2.

Raw science exposures and the associated raw calibration files were retrieved from the ESO science archive. We reduced the data of all four fields using the standard ESO MUSE pipeline (v.2.8.4; Weilbacher et al. 2020), and applied an additional sky subtraction in the final combined cubes using the median sky spectrum obtained from object-free regions in each field.

The pipeline-generated variance cube has been known to underestimate the data uncertainties (e.g. Bacon et al. 2017). Using the wavelength range of 6000–7000 Å, we obtained an empirical estimate of the uncertainties in each field and found that on average this empirical noise level is ≈1.6 times higher than the noise level inferred from the pipeline generated variance cube. We, therefore, scaled up the pipeline-produced variance cube by a factor of 1.6^2. This correction factor is similar to what has been adopted in previous studies (e.g. Borisova et al. 2016; Sanderson et al. 2021).

3.2 QSO light subtraction

To better reveal the emission from the extended nebulae, we removed the QSO light following a method similar to the high-resolution spectral differential imaging technique discussed in Haffert et al. (2019) and Xie et al. (2020). Below we briefly describe the main steps.

We first constructed a QSO template spectrum using the mean spectrum from the central 5 spaxels (i.e. within a radius of 0.2 arcsec) around the QSO. Next, for each spaxel contaminated by the QSO light, we divided the data in this spaxel by the QSO template spectrum to obtain a ratio spectrum. We then smooth this ratio spectrum with a median rolling filter with a window width of ~100 spectral pixels (i.e. ~125 Å). The exact window size is decided through trial and error and is slightly different for different fields. This smoothing step will maintain the low-order variation in the ratio spectrum while removing high-order features, such as strong emission lines and noise. Finally, we scale the QSO template spectrum by the smoothed ratio spectrum and subtract it from the spaxel to remove the QSO contamination. These steps were repeated for every spaxel within a radius of 30 pixels (i.e. 6 arcsec) from the QSO centre in each field.

Comparing with other commonly used QSO light subtraction methods, such as principle component analysis (and similarly, non-negative matrix factorization; e.g. Johnson et al. 2018; Helton et al. 2021) and a joint analysis of the QSO spectrum and the host galaxy spectrum incorporating stellar population synthesis models (e.g. Rupke, Gültekin & Veilleux 2017), the method described above has the advantage of being relatively simple while delivering very clean residual spectra. However, a couple of caveats should also be noted. By using a QSO template spectrum that is scaled according to the smoothed ratio spectrum, this method removes all low-order features, including continuum and broad emission lines, indiscriminate to the origin of such features. As a result, it removes the low-order signal from the QSO host galaxy as well as other possible continuum sources located underneath the QSO PSF. Hence, this method works well for revealing spectral features narrower than typical QSO broad lines, such as the extended nebula emission studied here, but it is not suitable for studies of host galaxies and continuum sources. Meanwhile, in the QSO template spectrum constructed around the core region of the QSO PSF, there are possible contributions from the template to the targeted narrow emission line, and therefore the line flux in the nebula after QSO light subtraction could be underestimated. We, therefore, take extra caution when forming the QSO template and exclude spaxels with relatively strong narrow signals at the wavelength of the lines of interest.

3.3 Narrow-band images

Additional continuum subtraction was applied to the full data cube across the FOV to further remove background continuum flux in spaxels not included in the QSO light subtraction step. In general, we used a continuum spectrum determined through linear interpolation using the median value in a blue (red) window that was approximately [−3000, −1500] ([+1500, +3000]) km s^{-1} away from the expected line centre. In practice, based on the observed wavelength of the line of interest in each field, the spectral windows were adjusted to avoid noisy regions due to strong skylines and other artefacts in the data cube.

To enhance the SNR of the extended faint emission in the outskirts of each QSO nebula, we smoothed the data in the spatial dimension with a Gaussian kernel. The FWHM of the Gaussian kernel is chosen to be 3.5 pixels (i.e. 0.7 arcsec) for all four fields. In Table 2, we list the atmospheric seeing size for each field measured at the position of the QSO at 7000 Å before applying the additional spatial smoothing. The total PSF FWHM after smoothing was ≈50 per cent larger than the seeing disk. No additional smoothing was applied along the spectral dimension. The 1σ surface brightness limit in a single wavelength slice (i.e. width of 1.25 Å) at the observed wavelengths of the [O II] λλ 3727, 3729 and [O III] λ 5008 lines for each field ranges from approximately 6×10^{-20} erg s^{-1} cm^{-2} arcsec^{-2} to 3×10^{-19} erg s^{-1} cm^{-2} arcsec^{-2}, as listed in Table 3. TXS0206−048 has the lowest noise level at the observed [O II] λλ 3727, 3729 wavelength due to a significantly longer total integration time.

With the smoothed, continuum- and QSO light-subtracted data cube, optimally extracted narrow-band images were constructed for both [O II] λλ 3727, 3729 and [O III] λ 5008 lines for the three lower redshift fields. For TXS0206−048, the [O III] λ 5008 line is redshifted out of the MUSE spectral coverage and therefore no results based on [O III] λ 5008 are available. Optimal extraction using a 3D mask that takes advantage of the information along both the spatial and the spectral dimension was carried out to maximize the SNR in the resulting narrow-band images. Detailed descriptions of the procedure can be found in, e.g. Borisova et al. (2016) and Sanderson et al.

Table 3. Summery of emission properties in spatially extended QSO nebulae[a].

Field name	Surface brightness Limit[b]		Luminosity (erg s^{-1})		Nebula area (kpc^2)	
	[O II]	[O III]	[O II]	[O III]	[O II]	[O III]
PKS0454−22	2.3×10^{-19}	1.7×10^{-19}	1.9×10^{42}	2.2×10^{43}	1552	2202
J0454−6116	1.2×10^{-19}	2.4×10^{-19}	3.5×10^{42}	5.3×10^{42}	3821	2128
J2135−5316	1.4×10^{-19}	2.6×10^{-19}	2.5×10^{42}	9.2×10^{42}	1614	2190
TXS0206−048	6.3×10^{-20}	–	2.0×10^{43}	–	6239	–

[a]Luminosities and nebula sizes are summed over the areas used for the subsequent VSF analysis, which are smaller than the areas shown in Fig. 1. See velocity maps (e.g. Fig. 3) for the areas included in the VSF calculation. Note that for the nebula in TXS0206−048, the $r < 1$ arcsec region centred on the QSO contributes to $\approx$50 per cent of the total luminosity. Excluding this central region results in a luminosity estimate consistent with the reported value in Johnson et al. (2022).
[b]1σ limit in units of erg s^{-1} cm^{-2} arcsec^{-2} over a single wavelength slice (i.e. 1.25 Å) at the observed wavelength of the corresponding emission line.

(2021). In short, the 3D mask was created based on an SNR threshold chosen for each voxel (i.e. volume pixel) of the data cube, and the minimum number of consecutive spectral pixels in a given spaxel to be included in the mask. For this study, we chose a voxel SNR threshold of 1 and a minimum number of consecutive spectral pixels of 3. The narrow-band images constructed using such 3D masks are shown in Fig. 1 for all four fields.

3.4 Emission-line analysis and velocity measurements

To determine the line-of-sight velocities at different locations across the nebulae, we performed a line profile analysis by adopting a Gaussian profile convolved with an appropriate instrumental line spread function. For fields with both [O II] $\lambda\lambda$ 3727, 3729 and [O III] λ 5008 detections, we carried out the analysis of these two lines separately. The [O II] $\lambda\lambda$ 3727, 3729 doublet is mostly unresolved for all fields at the MUSE resolution. Furthermore, both the [O II] $\lambda\lambda$ 3727, 3729 and [O III] λ 5008 emission lines exhibit complex line profiles showing evidence for multiple velocity components, particularly in the inner regions closer to the QSOs. For some individual velocity components, spatial variation is observed in the [O III]/[O II] line ratio, leading to different flux-weighted mean velocities at the same locations for these two lines. We, therefore, decided to take a simpler approach and fit these two lines separately.

We adopted an MCMC approach to search for the best-fitting parameters of individual Gaussian components, which was implemented with the PYTHON module EMCEE (Foreman-Mackey et al. 2013). Compared with least-square-based fitting methods, an MCMC approach provides a more robust posterior probability density distribution for the model parameters, naturally accounting for non-Gaussian posteriors as well as upper/lower limits. For the [O II] $\lambda\lambda$ 3727, 3729 blended doublet, we only included one Gaussian component in the model profile for all spaxels, as the current MUSE data do not provide sufficient spectral resolution to break the degeneracy between the centroids of multiple velocity components and the doublet line ratios. For the [O III] λ 5008 line, we conducted the fitting with up to four independent Gaussian components and determined the number of components in each spaxel based on the Bayesian information criterion (BIC) (see e.g. Sharma 2017). We required that a complex model with more Gaussian components can be accepted only when its BIC value was smaller than the BIC value of a simpler model by at least 30. We chose this more stringent threshold than the commonly adopted value of ΔBIC > 10 because the spectra from the data cubes often displayed complicated noise spikes that were not fully accounted for in the error arrays, and a

more conservative approach was required to avoid overfitting when using multiple components.

However, as we will discuss in Section 4.4 and show in Fig. A8, for spaxels with multiple Gaussian components to model the observed [O III] λ 5008 line, adopting a flux-weighted mean velocity leads to similar VSF measurements as adopting a one-component model (i.e. ignoring the multicomponent nature of the line). For simplicity, we, therefore, opted to focus on the VSF measurements based on the one-component model even for spaxels with complex line profiles. We will present and discuss results from the multicomponent fitting process of the [O III] λ 5008 line in a subsequent paper.

3.5 VSF measurements

Before carrying out the VSF measurements, we performed a series of checks to ensure that the results are robust. First, we examined possible contamination resulting from overlapping continuum sources due to projection effects. In particular, a large velocity contrast would suggest that such continuum sources might not belong to the same dynamic system as the rest of the line-emitting gas, and therefore should be excluded from the VSF measurements. For the PKS0454−22 and TXS0206−048 fields, we used the archival broad-band *HST* data to identify continuum sources (Helton et al. 2021; Johnson et al. 2022). For the J0454−6116 and J2135−5316 fields, due to a lack of higher spatial resolution imaging data, continuum sources were identified using a MUSE white-light image. We flipped the white-light image of each field along the x-axis (using the QSO centroid as the centre), and subtracted the flipped image from the original image. Strong continuum sources underneath the QSO PSF will lead to a pattern of significant residual flux at the original locations of such sources paired with significant oversubtraction at their flipped locations. This method helps to identify sources that might be easy to miss due to the QSO PSF. Flipping along the y-axis of the image would have achieved the same effect. Out of the four fields, we only identified two strong continuum sources in the J0454−6116 field that stood out in the velocity map and excluded the spaxels inside a circular aperture centered on each of these two continuum sources. The size of the aperture was chosen to enclose most of the continuum flux. For the remaining three fields, the continuum sources overlapping with the nebulae showed consistent velocities with the rest of the nebulae, and no spaxels were excluded from the VSF measurements.

In addition, we masked spaxels with highly uncertain velocity measurements. Because we adopted a generous voxel SNR threshold when forming the 3D masks (see Section 3.3), some spaxels included in the line fitting step had relatively faint signals and large

measurement uncertainties that would significantly impact the VSF measurement uncertainties. We excluded spaxels with a velocity uncertainty larger than 45 km s^{-1}. This threshold was approximately two to three times the median uncertainty of the fitting results based on the [O III] λ 5008 line, and was about the median uncertainty for measurements based on the [O II] $\lambda\lambda$ 3727, 3729 line among all fields. We verified that changing this threshold by a small amount (i.e. $\pm$15 km s^{-1}) did not lead to significant differences in the subsequent analyses. Finally, we examined the probability density distribution of the observed velocities among the rest of the spaxels in each field, and filtered out spaxels that are outliers (i.e. either too blue or too red in velocity, defined to be the $\approx$2 per cent tail on both ends). We also excluded the central $r \leq 3$ pixels region for both J0454−6116 and J2135−5316 fields due to noisy residuals from the QSO light removal, which was not necessary for PKS0454−22 and TXS0206−048.

All spaxels left after the above filtering steps were included in subsequent VSF measurements. Summing over all these spaxels, we report the total luminosity in [O II] $\lambda\lambda$ 3727, 3729 and [O III] λ 5008 line emission as well as the total area (in kpc^2) for each field in Table 3. Out of the four fields, TXS0206−048 has the largest area. In fact, in terms of the area and the total line emission luminosity of the [O II] nebula, TXS0206−048 exceeds the 'Makani' nebula at $z = 0.459$, the largest [O II] nebula detected hitherto (Rupke et al. 2019).[1] The filtered [O II] velocity map of the TXS0206−048 field is shown in the left panel of Fig. 3, together with its corresponding velocity uncertainty map on the whole 3D mask footprint for comparison. The filtered velocity maps of the other three fields, for both [O II] and [O III] lines, are shown in Figs A1–A6 in the Appendix.

Because of the spatial correlation between adjacent spaxels, when measuring the VSF, individual velocity pairs within a distance separation bin are not independent of each other. We therefore cannot directly propagate the measurement uncertainties of the velocity centroids in each spaxel to estimate the uncertainties of the VSFs. To robustly estimate the uncertainty of the VSF, we proceeded with the following steps. First, we divided the whole nebula in each field into smaller subregions. The size of these subregions was roughly the FWHM of the total PSF in each field (see Table 1). Most of these subregions were squares while some subregions located near the edge of the nebula had irregular shapes. Next, we randomly selected one spaxel per subregion and constructed a VSF based only on the selected spaxels. We then repeated the step of randomly selecting one spaxel per subregion 1000 times, and each time obtained a VSF measurement. In addition, for each iteration, we perturbed the velocity map to within the measurement uncertainties by randomly assigning a new velocity value drawn from the MCMC chain to each spaxel. By restricting the pair formation to one spaxel per subregion defined by the PSF, we were able to minimize correlated noise between adjacent bins in the VSF and recover small-scale power lost due to smoothing. We refer to this procedure as a modified bootstrap method. We obtained a mean and standard deviation of the 1000 VSFs as the measurement and associated uncertainty of the final VSF. Note that while all VSFs were measured using a distance bin size of one spaxel, only measurements separated by scales larger

than the size of the total PSF were included when quantifying the slope of the VSFs (see Section 4.1 for details of constraining the VSF slopes).

4 RESULTS

Of the four QSO nebulae studied here, TXS0206−048 has the most constraining IFS data and the largest spatial extent (see Fig. 1 and Table 3). Together, these characteristics ensure the best-determined velocity map and well-constrained VSFs. In this section, we present the VSFs measured for extended QSO nebulae at $z_{QSO} \approx 0.5$–1.1 with a focus on the line-emitting gas detected around TXS0206−048 at $z_{QSO} \approx 1.1$. In addition, we investigate the impact on the observed VSFs due to possible underlying coherent bulk flows in these nebulae. We consider the presence of unidirectional velocity gradient, radial, and tangential motions in the observed velocity field of each nebula, and compare the measured VSFs before and after removing these smooth velocity components.

4.1 The observed VSFs of TXS0206−048

The velocity and velocity uncertainty maps of the [O II] $\lambda\lambda$ 3727, 3729 nebula around TXS0206−048 displayed in Fig. 3 show that the line-emitting gas is highly disturbed with well-determined line-of-sight velocities spanning a wide range from $\approx$−150 km s^{-1} to $\gtrsim$300 km s^{-1} across the full extent of nearly 200 kpc defined by the narrow stream-like feature towards the northeast and southwest (Johnson et al. 2022). However, most of the statistical power in the VSF measurements lies in the main, more spherically distributed nebula of $\approx$90 kpc in diameter centred on the QSO. The observed second-order VSF, S_2', is well characterized by a single power-law scaling up to $r_{proj} \approx 60$ kpc over the projected distance range from $r_{proj} < 6$ kpc to $r_{proj} \approx 60$ kpc (Fig. 3).

To quantify the second-order VSF slope, we apply a power-law model convolved with the total PSF to characterize the reconstructed S_2' from each of the 1000 realizations obtained through the modified bootstrap method described above. We adopt a Gaussian function with an FWHM of 8.3 kpc for the PSF in TXS0206−048 (see Table 1), and we follow the steps discussed in Section 2 to calculate the shape of the power-law model after the PSF convolution. Note that we only consider non-negative power-law slopes, as negative slopes are not motivated by the data here and would lead to divergence at $r = 0$ for a simple power-law parametrization. The model fitting is done over the distance range of 8.3 kpc $< r_{proj} < 60$ kpc, using the Scipy curve_fit routine. The small-scale cut-off at 8.3 kpc is to minimize systematic uncertainties due to spatial smoothing, while the large-scale threshold at 60 kpc is determined based on a series of trials and errors to optimize the fitting precision and accuracy. For S_2 of TXS0206−048 obtained using the [O II] $\lambda\lambda$ 3727, 3729 emission line, we measure a slope of $\gamma_2 = 0.72^{+0.12}_{-0.11}$. The best-fitting value corresponds to the median value among the 1000 fitting results, and the 16th and 84th quantiles represent the lower and upper limit, respectively.

In Fig. 3, the best-fitting model is shown in the blue solid curve, with the dark (light) blue shaded region representing the 16th–84th (2nd–98th) quantile range for the models. This measurement is consistent with the Kolmogorov slope of 2/3 (orange dashed curve in Fig. 3) for isotropic, homogeneous, and incompressible turbulence. We have experimented with removing the stream-like features both north- and south-ward of the main nebula, and we obtained consistent VSF measurements.

---

[1]Note that the size and [O II] line luminosity of TXS0206−048 reported in Table 3 were obtained at a surface brightness level of $\sim$10^{-19} erg s^{-1} cm^{-2} arcsec^{-2}, significantly lower than the surface brightness threshold of 5×10^{-18} erg s^{-1} cm^{-2} arcsec^{-2} used in Rupke et al. (2019). At the level of 5×10^{-18} erg s^{-1} cm^{-2} arcsec^{-2}, the TXS0206−048 [O II] nebula has an area $\approx$4100 kpc^2, slightly smaller than 4900 kpc^2 covered by 'Makani'.
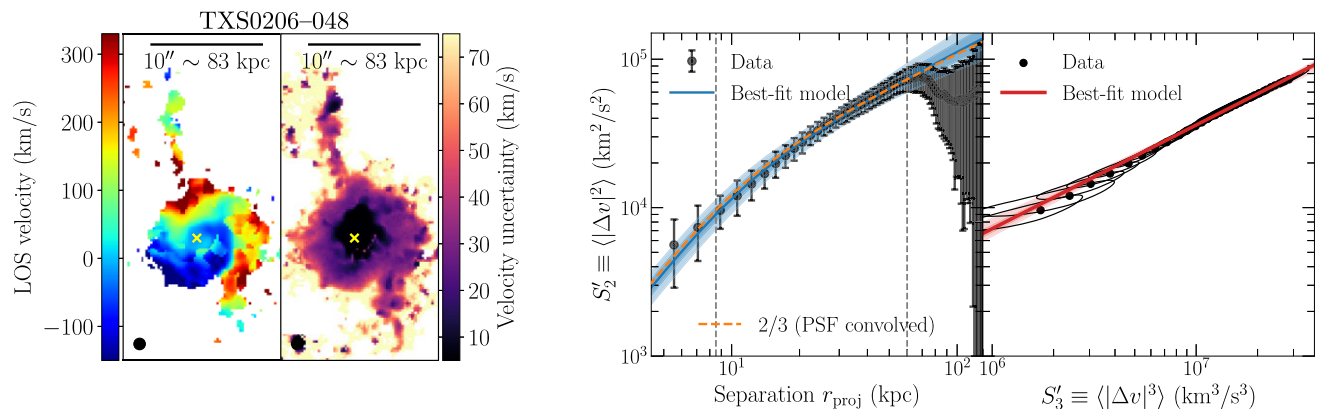
Figure 3. *Left-hand panels:* The observed velocity map and the associated measurement uncertainties of the extended nebula around TXS0206−048 using the [O II] λλ 3727, 3729 emission lines. The yellow cross in both panels marks the QSO position. Only pixels included in the VSF calculation are shown in the velocity map (see Section 3.5), while the velocity uncertainty panel contains all pixels from the 3D mask (see Section 3.3). The black circle at the bottom left represents the total PSF of this field, after convolving the atmospheric seeing with the smoothing kernel applied to improve the SNR. *Right-hand panels:* The second-order VSF $S_2'(r)$ constructed using the velocity map displayed in the left-hand panel, along with the S_2' vs. S_3' correlation. Vertical dashed lines mark the fitting boundaries in r_{proj}, with the left line indicating the $FWHM_{total}$ of the field and the right line indicating the maximum r_{proj} beyond which a single power-law model does not provide a good fit anymore. The best-fitting model of S_2', after being convolved with the total PSF, is shown as the blue solid curve. The dark (light) blue-shaded region represents the 16th–84th (2nd–98th) quantile range for the model. The orange dashed curve shows the PSF-convolved Kolmogorov mode for S_2' with a theoretical slope of $\gamma_2 = 2/3$. In the right-hand panel, the best-fitting power-law model for the S_2' versus S_3' relation is shown as the red solid line with the model uncertainty represented by the red-shaded region. Only the data points within the same distance separation range for the fitting of S_2' are shown in the S_2'–S_3' panel, with the ellipses showing the correlated 1σ error area determined by the eigen vectors and eigen values of the covariance matrix within each distance bin. We measure an intrinsic power-law slope of $\gamma_2 = 0.72^{+0.12}_{-0.11}$ and $\gamma_3 = 1.03^{+0.18}_{-0.16}$ for S_2 and S_3, respectively (see Table 4).

In addition to S_2', for each of the 1000 modified bootstrap samples described above, we also calculate the VSF S_p' for other orders up to $p = 6$, and examined if the ESS discussed in Section 2 applies to this data set. Limited by the data quality, VSFs for $p > 6$ become too noisy to result in meaningful constraints. In the rightmost panel of Fig. 3, we show the measurement of S_2' as a function of S_3' for TXS0206−048. Note that the S_2' and S_3' measurements are highly correlated. Therefore, we use ellipses to show the 1σ confidence intervals with the elongations and sizes determined by the eigen vectors and eigen values of the data covariance matrix in each distance bin.

Similar to the ESS presented in Benzi et al. (1993, see their fig. 3), we observe a well-defined power-law relation of $S_2' \propto S_3'^{0.70\pm0.03}$. The measurement of this power-law slope is obtained using the 1000 realizations of the velocity map, and only the data points within the same distance range of 8–60 kpc are included in the model fitting. Due to the tight correlation between S_2' and S_3', the ESS scaling slope is much better constrained than the individual slopes γ_2 and γ_3. Because we can analytically incorporate the effect of PSF smoothing into a power-law S_2 but not for S_3, the presence of the ESS in this data set conveniently allows us to measure a slope and amplitude of S_3 accurately. In addition, as discussed in Section 2, the smoothing effect does not change the power-law scaling relation for ESS. Combining the measured S_2 slope of $\gamma_2 = 0.72^{+0.12}_{-0.11}$ and the S_2-S_3 power-law scaling of $\gamma_2/\gamma_3 = 0.70 \pm 0.03$, we obtain a slope of $\gamma_3 = 1.03^{+0.18}_{-0.16}$ for S_3 in TXS0206−048. Consistent with the result for S_2, the S_3 slope is in excellent agreement with the expectation of $\gamma_3 = 1$ for Kolmogorov turbulence. Discussions on the slopes of higher order VSFs are presented in Section 5.3.

4.2 Effect of large-scale velocity gradients

While the measured S_2 and S_3 are both consistent with Kolmogorov turbulence for the nebula surrounding TXS0206−048, a caveat

remains regarding the presence of large-scale coherent flows which could contribute to the observed power in the velocity structure functions (e.g. Zhang et al. 2022 for a discussion). In this section, we address this issue by considering a unidirectional flow model for removing the bulk flow in the observed velocity map.

We first adopt a simple model velocity map parametrized as $v(x, y) = ax + by + c$, where x and y are the coordinates of individual spaxels within the nebula, and a, b, and c are free parameters used to capture any potential large-scale velocity gradient. We apply this model to the empirical velocity map displayed in the left-most panel of Fig. 3, and obtain the best-fitting velocity gradient map as shown in the left-most panel of Fig. 4. The gradient in the model is ≈ 3.7 km s^{-1} kpc^{-1}. We estimate the uncertainty of this gradient by fitting 1000 velocity maps that are randomly generated based on the MCMC line fitting chain for each spaxel. Due to the relatively large number of spaxels included in the analysis (i.e. over 2000 in the field of TXS0206−048), the velocity gradient based on this simple three-parameter model is well determined. We then subtract the best-fitting 2D velocity gradient from the original velocity map and obtain the residual velocity map shown in Fig. 4.

At first look, the best-fitting unidirectional flow model does not completely capture the coherent flows displayed in Fig. 3. While it captures the apparent velocity shear along the east-west direction, the velocity gradient visible along the north-south direction remains. This motivates a different approach to consider the presence of radial/tangential flows, which is discussed in Section 4.3 below. Here we proceed with the discussion using the residual map displayed in Fig. 4. We repeat the VSF measurements described in Section 3.5 and obtain both the S_2' and the S_2'–S_3' ESS relation. The results are shown in the right-hand panels of Fig. 4.

As expected, subtracting a large-scale velocity gradient has a larger impact on larger scales, and S_2', in general, becomes flatter compared to the results in Fig. 3 using the original velocity map. Instead of continuing to rise to larger scales, S_2' appears to flatten
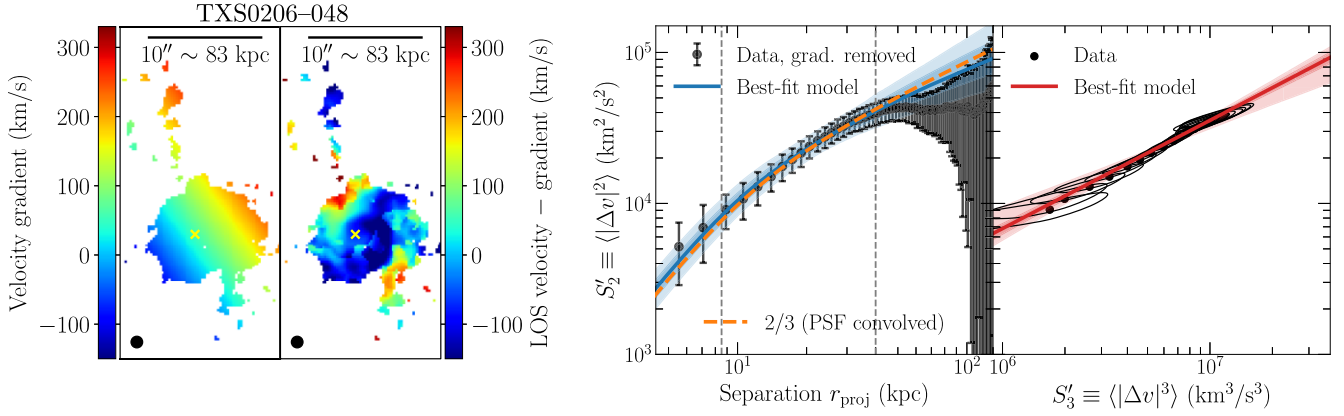
Figure 4. *Left-hand panels:* The best-fitting 2D velocity gradient model and the residual velocity map after subtracting the velocity gradient from the observed velocity map for TXS0206−048. The yellow cross in both panels marks the QSO position. Similarly to the left-most panel of Fig. 3, only pixels included in the VSF calculation are shown. *Right-hand panels:* $S_2'(r)$ and the S_2'–S_3' ESS relation constructed using the gradient-subtracted velocity map displayed on the left. Similar to the right-hand panels of Fig. 3 but calculated with the gradient removed velocity map. We measure an intrinsic power-law slope of $\gamma_2 = 0.56^{+0.16}_{-0.17}$ and $\gamma_3 = 0.78^{+0.28}_{-0.25}$ for S_2 and S_3, respectively (see also Table 4).

at $r_{\mathrm{proj}} \approx 40$ kpc. The S_2' versus S_3' ESS still holds for the gradient removed velocity map. We estimate an intrinsic power-law slope of $\gamma_2 = 0.56^{+0.16}_{-0.17}$ for S_2 and $\gamma_3 = 0.78^{+0.28}_{-0.25}$ for S_3. Note that the fitting range is now restricted to 8.3 kpc $< r_{\mathrm{proj}} < 40$ kpc due to the flattening at 40 kpc, resulting in larger uncertainties in the best-fitting slopes. While the slope is flatter than what is obtained before removing the velocity gradient model, the two results are consistent to within the uncertainties. Similarly, we also overplot the expected Kolmogorov S_2' with a slope of 2/3 after convolving with the PSF as the orange dashed curve in Fig. 4. It is clear that despite the data points exhibiting a flatter overall trend, the measurements still agree with the Kolmogorov slope over the scales probed.

Based on the morphology of the nebulae (see Fig. 1) and the velocity measurements, the nebulae in all four fields do not show signatures of well-established rotation disks. We, therefore, do not consider a more elaborate disc model with additional parameters such as inclination and maximum rotation velocity.

4.3 Effects of radial and tangential motions

Complementary to the simple, unidirectional coherent flows discussed above, here we investigate whether there exist significant differences between the VSFs constructed along the radial versus tangential directions. This is a physically motivated scenario as gas outflows can manifest as coherent, radial motions while gas infalls are more likely to form large-scale tangential motions due to the conservation of angular momentum. For instance, if a nebula is mostly comprised of isotropic supergalactic winds, we would expect that the measured S_2 is driven by the power associated with radial motions with the best-fitting slope γ_2 indicative of the acceleration of the wind. In addition, this test can also reveal anisotropy if the radial versus tangential VSFs exhibit distinctive shapes.

Using the velocity map presented in Fig. 3, we classify the velocity pairs into two groups based on their spatial configuration with respect to the QSO location. The classification criterion is illustrated in the left-hand panel of Fig. 5. In this classification, we require both pixels in a pair to reside in the same quadrant of the nebula with the angle ϕ (see Fig. 5) being equal to or smaller than 90°. Velocity pairs taken from pixels located in different quadrants of the nebula are not considered to avoid ambiguities between radial and tangential
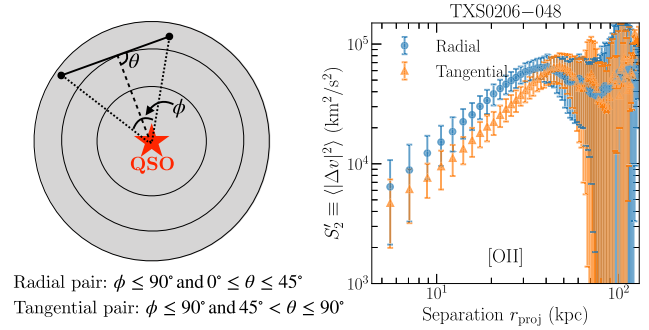

Figure 5. *Left:* Illustration of the radial versus tangential pair classifications. *Right:* The second-order VSFs S_2' measured using radial and tangential pairs, respectively, based on the velocity map presented in Fig. 3. The shapes of S_2' for the radial and tangential pairs are consistent with each other, while the radial pairs exhibit a higher amplitude in the VSF.

pairs. We then calculate θ, which is the angle between the vector that connects the two points in a pair and the vector that connects the pair mid-point to the QSO location, as shown in Fig. 5. We assign any pairs with $0° \le \theta \le 45°$ ($45° < \theta \le 90°$) as radial (tangential) pairs, and repeat the VSF measurements using these two groups of pairs separately. The results are shown in the right-hand panel of Fig. 5.

The shapes of S_2' for the radial and tangential pairs are consistent with each other, while the radial pairs exhibit a slightly higher amplitude in the VSF. This test demonstrates that the nebula gas undergoes dynamical processes with similar turbulence energy cascade characteristics along the radial and tangential directions, and that both directions have comparable contributions to the signal in the total VSF presented in Fig. 3. Repeating this exercise with the gradient-removed velocity map leads to the same conclusion.

4.4 The observed VSFs of PKS0454−22, J0454−6116, and J2135−5316

For the remaining three fields PKS0454−22, J0454−6116, and J2135−5316, both the [O II] $\lambda\lambda$ 3727, 3729 and [O III] λ 5008 lines are detected in the MUSE cubes. We present the VSF measurements

based on both lines, which are shown in Figs A1–A6 in the Appendix. Constraints on the slopes of the VSFs are summarized in Table 4.

Compared with the results for TXS0206−048, the constraints on the slopes of the VSFs for these three QSO nebulae are weaker. The large uncertainties can be attributed to the limited dynamic range in spatial scale when comparing the spatial extent of the line-emitting nebulae with the size of the PSF in the data (see Section 2). As listed in Table 3, the [O II] nebula included in the VSF measurements for TXS0206−048 is ≈2–4 times larger than that of these three fields. The larger area leads to smaller uncertainties in the VSF measurements in each distance bin, and a larger dynamic range in distance separation, both contributing to a better constrained VSF. In contrast, a limited dynamic range in the pair separations for the remaining three nebulae inevitably pushes the VSF measurements closer to the injection scale, where we expect the VSF to flatter (e.g. Benzi et al. 1993). If this is the case, then no robust constraints can be obtained for the VSF slopes in the inertial range.

Similar to the result of TXS0206−048, removing a large-scale unidirectional velocity gradient from the velocity maps results in a flatter VSF. However, the measured slopes are consistent before and after the gradient removal, particularly with the large uncertainties for these fields. The VSFs calculated with radial vs. tangential pairs are also consistent in terms of the general shape and amplitude within each field, as shown in Fig. A7. Despite poorly constrained S_2', a strong correlation between S_2' and S_3' remains with $\gamma_2/\gamma_3 \approx 0.7$ (see Figs A1–A6).

4.5 Effects of line-of-sight projections

The availability of both [O II] $\lambda\lambda$ 3727, 3729 and [O III] λ 5008 emission signals for three of the QSO nebulae studied here also offers an opportunity to investigate the effect of line-of-sight projection. In particular, while velocity measurements of [O II] $\lambda\lambda$ 3727, 3729 and [O III] λ 5008 for PKS0454−22, J0454−6116, and J2135−5316 are mostly consistent with each other, there are regions with significantly different values between the two velocity maps, revealing not only that the emission signals are a blend of multiple components along the sightline but also that there exists a large variation in the [O III]/[O II] line flux ratio between different components. Such variations indicate changing ionization conditions between different gas clumps that overlap along the line of sight and/or are unresolved along the plane of the sky (see Section 5.4 for further discussion).

Here, we test how the measured VSFs change with different treatments of regions showing multicomponent [O III] λ 5008 line profiles. Specifically, we compare three different scenarios where we assign to each multicomponent spaxel (1) the velocity of the component with the largest line flux, (2) the velocity obtained by forcing a one-component fit, and (3) the flux-weighted mean velocity across all components. We present the VSF comparison under these three scenarios in Fig. A8. While the uncertainties are large, this data set indicates that using the velocity of the dominant component in flux for multicomponent spaxels may lead to a flatter VSF with higher amplitudes on small scales. Using the flux-weighted mean velocity and adopting a one-component fitting velocity results in similar VSFs, which motivates our decision to present the single-component fitting result in the VSF measurements.

5 DISCUSSION

Of the four QSO nebulae studied in this work, we have shown that the VSFs of one QSO nebula, TXS0206−048, are in spectacular agreement with expectations from the Kolmogorov law.

The Kolmogorov model applies to isotropic, homogeneous, and incompressible flows. The observed agreement, therefore, implies that gas flows in the nebula are subsonic and that the turbulent energy is being transferred at a constant rate between different spatial scales. Given the expectation that the observed [O II] emission traces cool gas of temperature $T \sim 10^4$ K with a sound speed of $c_s^{\text{cool}} \approx 10$ km s^{-1}, the observed velocity difference of $\Delta v \gtrsim 100$ km s^{-1} on scales greater than 10 kpc would lead to a conclusion of supersonic motions within the cool gas. On the other hand, the QSO is found to reside in a massive halo of $M_{\text{halo}} \approx 5 \times 10^{13}$ M$_\odot$ (see Section 5.1) with an anticipated temperature of $T \sim 10^7$ K for the hot halo and a sound speed of $c_s^{\text{hot}} \approx 300$ km s^{-1}. If the [O II]-emitting gas originates in cool clumps condensed out of the surrounding hot halo, then the observed VSFs capture the subsonic motions of individual clumps relative to the hot medium. For the remaining three nebulae around PKS0454−22, J0454−6116, and J2135−5316, however, no robust constraints for the VSFs can be determined due to a limited dynamic range in seeing-limited data.

In this section, we discuss the implications for the energy balance in the diffuse CGM in these QSO host nebulae. We first estimate the turbulence energy transfer rate, using TXS0206−048 as an example, and explore possible causes for the observed differences in the VSFs between the different QSO nebulae. Finally, we review the limitations and caveats in the observations.

5.1 Constant turbulent energy cascade in TXS0206−048

For turbulent gas that follows the Kolmogorov law, the mean energy transfer rate per unit mass ϵ is expected to be constant within the inertial range and can be estimated following

$$\epsilon = \frac{5}{4} \left[\frac{|\langle (\Delta v(r)^3) \rangle|}{r} \right] \approx \frac{5}{4} \left[\frac{\langle |\Delta v(r)|^3 \rangle}{r} \right]. \tag{8}$$

This is commonly referred to as the 'four-fifths law' in fully developed turbulence, and is an exact result derived from the Navier–Stokes equations (Kolmogorov 1941; Frisch 1995). As stated in Benzi et al. (1993), the relation $|\langle \Delta v(r)^3 \rangle| \approx \langle |\Delta v(r)| \rangle^3$ is not obvious from first principles but has been experimentally verified. Using the S_3 measurement for TXS0206−048, we obtain $\epsilon \approx 0.2$ cm^2 s^{-3}. This energy transfer rate is comparable to the value measured with H α filaments in the Perseus cluster (Li et al. 2020), as well as the 0.1–1 cm^2 s^{-3} rate estimated for the Orion Nebula (e.g. Kaplan & Pikelner 1970). Rauch et al. (2001) reported a lower ϵ of $\sim 10^{-3}$ cm^2 s^{-3} for C IV absorbers at $z \approx 3$, suggesting that the CGM in high-redshift star-forming halos is less turbulent with a lower energy cascade rate (see also Rudie et al. 2019). However, due to the unspecified uncertainty in the VSF measurement in Rauch et al. (2001) and the different data set used, it is not conclusive whether the current discrepancy between our result and that of Rauch et al. (2001) is significant.

Figs 3 and 4 show that the VSF of TXS0206−048 flattens at around 50 kpc. Given that the statistical uncertainty in the VSF does not increase significantly until a scale of ≈80 kpc, the turnover point at 50 kpc may be interpreted as the energy injection scale in this system. In contrast, we do not detect signatures of the dissipation scale in all systems due to a fundamental limitation on the spatial resolution in seeing-limited observations.

In addition, the estimated ϵ suggests that turbulent energy is subdominant in QSO host halos, as can be shown through the following calculations. The total mass of the dark matter halo hosting TXS0206−048 is estimated to be $M_{\text{halo}} \approx 5 \times 10^{13}$ M$_\odot$ (Johnson et al. 2022). Adopting a baryon fraction of $f_b \approx 0.15$ (Planck Collaboration I 2020), we calculate a total baryonic mass within a radius of 50 kpc

Table 4. Summery of the power-law slopes of the VSFs constructed using [O II] and [O III] lines[a].

Field name	[O II] γ_2	[O II] γ_3	[O II] Grad. removed[b] γ_2	[O II] Grad. removed[b] γ_3	[O III] γ_2	[O III] γ_3	[O III] Grad. removed[b] γ_2	[O III] Grad. removed[b] γ_3
PKS0454−22	<0.78	<1.15	<0.66	<0.99	<0.67	<0.94	<1.45	<2.3
J0454−6116	<0.51	<0.77	<0.45	<0.74	<0.84	<1.26	<0.33	<0.48
J2135−5316	<0.50	<0.76	<0.65	<1.02	<1.23	<1.81	<1.12	<1.75
TXS0206−048	$0.72^{+0.12}_{-0.11}$	$1.03^{+0.18}_{-0.16}$	$0.56^{+0.16}_{-0.17}$	$0.78^{+0.28}_{-0.25}$	–	–	–	–

[a]Constraints for the best-fitting slopes listed here are based on the 1000 modified bootstrap samples (see Section 3.5). These slopes are the intrinsic power-law slopes for S_2 and S_3, as our fitting procedure explicitly accounts for the smoothing effect in the measured S'_2 and S'_3 (see Section 4.1). For PKS0454−22, J0454−6116, and J2135−5316, we present 95 per cent upper limits for the slope under the assumption that the observed pair separations are within the inertial range. If the available pair separations are close to injection scales, then no robust constraints can be obtained. For TXS0206−048, we list the median value as well as the 16th and 84th quantiles as lower and upper limits. Note that, as discussed in Section 4.1, we only consider non-negative power-law slopes.
[b]Measurements obtained after removing a 2D velocity gradient (see Section 4.2).

to be $\sim 3 \times 10^{11}$ M$_\odot$ for an NFW halo with a reasonable choice of halo concentration (i.e. between 4 and 10). This gives us a total turbulent energy transfer rate of $\dot{E}_{\text{turb}} \sim 10^{44}$ erg s^{-1}, assuming that gas of all phases is perfectly coupled dynamically and that the turbulence cascade does not affect gas residing at distances much larger than ≈ 50 kpc (i.e. the injection scale) from the halo center. Keeping these assumptions in mind, the turbulent energy that will eventually dissipate and heat up the gas in the CGM is ~ 0.05 per cent of the bolometric luminosity of the QSO (see Table 1), which is similar to the wind energy fraction observed in AGN outflows (e.g. Fabian 2012; Sun, Greene & Zakamska 2017). At the same time, this turbulent heating rate has the same order of magnitude as the [O II] $\lambda\lambda$ 3727, 3729 line luminosity. As we expect the gas to also cool through other forms of emission (e.g. [O III] λ 5008, H α and Ly α lines for the $\sim 10^4$ K ionized phase), the turbulent heating rate is not sufficient to offset cooling of this gas in the vicinity of a luminous QSO.

Finally, we note that in comparison to the remaining three QSO nebulae included in this study (see Table 1), TXS0206−048 occurs at the highest redshift QSO, $z_{\text{QSO}} \approx 1.13$, and appears to reside in the highest-mass halo with a significant number of group members being super-L_* galaxies and a large velocity dispersion (Johnson et al. 2022). The associated galactic environment may also play a significant role in driving the turbulence in the CGM, in addition to QSO outflows.

5.2 Implications of the VSF slopes

While the Kolmogorov theory has explicit predictions for the slopes of the VSF, a number of factors can impact the empirical measurements and should therefore be taken into account when interpreting the results. As discussed in Section 2, if the thickness of the nebulae along the line of sight is larger than the scales probed in the VSF, the projection effect will steepen the VSF. If the nebulae identified around these four QSOs are more sheet-like than spherical, then we would expect the intrinsic slope to be flatter than measured. Of the four nebulae studied here, J2135−5316 exhibits an elongated morphology and is most likely affected by such projection effect.

One possible explanation for the flat slopes is the presence of dynamically important magnetic fields, where the kinetic energy cascade is suppressed due to magnetic tensions (e.g. Boldyrev 2006; Brandenburg & Lazarian 2013; Grete, O'Shea & Beckwith 2021; Mohapatra et al. 2022). Another interesting scenario for flattened VSFs is one where energy injections happen at multiple different length scales, instead of one scale that defines the canonical upper limit of the turbulent inertial range. When combining multiple kinetic

energy power spectra with different injection scales, the resulting VSF reflects the superposition of the different components, leading to a flatter slope due to elevated power at scales smaller than the largest injection scale of the system (e.g. ZuHone, Markevitch & Zhuravleva 2016). This scenario is consistent with a diverse range of dynamical processes expected to be present in the CGM of a QSO halo, such as gas outflows, mergers, AGN-inflated bubbles, and relativistic jets (e.g. Fabian 2012). While the detailed mechanisms through which these processes transfer kinetic energy to the gas are poorly understood at the current moment, it is likely that different processes have different characteristic scales for energy injection. Irrespective of what the detailed mechanisms are, if the pair separations are indeed closer to the injection scale, then no conclusive constraints can be obtained for the VSF slopes in the inertial range.

Alternatively, the range of VSF slopes across the four fields could also be suggestive of a time-dependent evolution of these nebulae. As the energy injection from QSO outflows is expected to be episodic, turbulent energy may be dissipated during the off cycle, leading to a flat VSF. For virialized systems with a complete absence of turbulence, Melnick et al. (2021) indeed obtains flat VSFs based on N-body simulations. Taking TXS0206−048 as a reference, turbulent energy on scales of ~ 50 kpc is expected to be dissipated on a time scale of $\langle |\Delta v|^2 \rangle / \epsilon \sim 100$ Myr, and the time scale will be shorter for smaller spatial scales. Under this scenario, the observed flatter VSFs in the three lower redshift QSO nebulae suggest that the most recent episode of significant energy injection occurred more than ~ 100 Myr ago. Because such time scale exceeds the typical QSO lifetime of $\sim 0.1-10$ Myr (e.g. Schawinski et al. 2015; Sun et al. 2017; Shen 2021), this would make the radiative feedback during the luminous phase of an AGN an unlikely source for driving the observed turbulence.

At the same time, recall that the four QSOs reside in a diverse range of galactic environments, with TXS0206−048 in a rich dynamic galaxy group while J2135−5316 in a relatively isolated environment with only two neighbouring galaxies found (see Table 1). If galaxy/satellite interactions are a main driver of the turbulent CGM, then a flat VSF found for J2135−5316 may be attributed to the quiescent state of its galactic environment.

5.3 Extended self-similarity scaling slopes

In addition to the slopes γ_p of individual VSFs, the ESS scaling slopes between different orders can also shed light on the dynamic state of the gas. We have measured the slopes of VSFs of each nebulae for up to $p = 6$. As mentioned in Section 4.1, with the current data set, VSFs for $p > 6$ become too noisy to deliver meaningful constraints. The results are presented in Fig. A9, along with theoretical expectations

presented in She & Leveque (1994) and Boldyrev (2002). These models account for Kolmogorov turbulence with the intermittency correction and supersonic magnetohydrodynamic turbulence, respectively. The simulation results for transonic and supersonic hydrodynamic turbulence presented in Pan & Scannapieco (2011) are also included in Fig. A9 for comparison.

It is clear that the strongest discriminating power between these different scenarios lies in the higher order VSFs with $p \geq 4$. Due to large uncertainties in our measurements particularly for higher orders, we can only rule out the scenario for supersonic hydrodynamic turbulence with a Mach number of 6.1 from Pan & Scannapieco (2011). While the measurements appear to support the presence of subsonic turbulence in all four quasar nebulae, we note that the simple $p/3$ scaling relative to S_3 is also expected from a simple dimensional inference. Consequently, in the absence of direct measurements of S_2, the relative scaling between different orders alone does not provide conclusive evidence for whether or not the gas follows subsonic turbulence.

5.4 [O II] and [O III] surface brightness profiles

As mentioned in Section 4.5, examinations of the observed [O III]/[O II] line flux ratio across the nebulae have revealed intrinsic differences in the gas traced by the [O II] and [O III] emission features. Here, we investigate the circularly averaged radial surface brightness profiles for [O II] and [O III] lines, as shown in Fig. 6, in order to gain insights into the difference in the spatial distribution of the gas probed by different emission features. The observed one-dimensional surface brightness profile also facilitates a direct comparison of the gas properties across the four fields and with high-redshift quasars. Similar to the practice in Borisova et al. (2016), to obtain a more robust uncertainty estimate for the surface brightness level, we use narrow-band images collapsed over a fixed range of wavelength slices across the whole field, instead of the optimally subtracted images shown in Fig. 1. The wavelength range used for the narrow-band images here is decided based on the largest range along the wavelength dimension in the corresponding 3D masks (see Section 3.3). We also manually remove additional residuals in the narrow-band images that are not associated with the nebulae. This step is necessary because taking the circularly averaged value within each annulus could pick out faint spurious signals, especially in the noise-dominated regions. For the areas that are filtered out in the VSF measurement step (see Section 3.5), we indicate their corresponding radii with vertical shaded regions in Fig. 6 to guide the visual comparison. For TXS0206−048, the vertical shaded region denotes where the stream structures away from the main nebula contribute significantly to the averaged surface brightness level.

We find a good fit for the [O II] emission with Sérsic profiles (Sersic 1968), with the best-fitting half-light radius $R_e \approx [10, 10, 9, 6]$ kpc and the best-fitting Sérsic index $n \approx [1.1, 2.6, 2.5, 3.0]$, for the four fields with increasing redshifts. The best-fitting models for the [O II] profiles are shown in dotted curves in Fig. 6. For the [O III] profiles, however, we cannot find a good fit with Sérsic, exponential, or cored isothermal profiles. Instead, a single power-law with a slope of ≈ -3 can provide a good match to the [O III] profiles, except for the flat core regions (approximately inner 10 kpc) of J0454−6116 and J2135−5316. We therefore simply overplot this power law with a slope of -3 in Fig. 6 for comparison. This slope also roughly matches the slopes of the [O II] profiles outside of the core region.

Note that the [O II] and [O III] surface brightness profiles in the optical nebulae here are much steeper than the spatial profiles observed in extended Ly α nebulae around $z \approx 3$ QSOs, which have

characteristic power-law slopes of ≈ -2 (e.g. Steidel et al. 2011; Borisova et al. 2016; Arrigoni Battaia et al. 2019). This contrast in slope between optical nebulae and Ly α nebulae can be explained by the resonant nature of Ly α photons, resulting in more extended Ly α emission with shallower spatial profiles compared with the continuum and non-resonant line emission (e.g. Steidel et al. 2011; Wisotzki et al. 2016; Patrício et al. 2016; Leclercq et al. 2017; Chen et al. 2021).

In the right-most panel of Fig. 6, we show the [O III]/[O II] line flux ratios as a function of radial distance from the QSOs for the three lower redshift fields. Here, we see the manifestation of the extreme ionization condition in the vicinity of these bright QSOs, with the line ratios far exceeding the nominal values of [O III]/[O II]<1 for typical star forming and even AGN regions (e.g. Kewley et al. 2001; Kauffmann et al. 2003). Particularly for PKS0454−22, the [O III]/[O II] ratio is significantly enhanced in the central 10 kpc, reaching a value of ≈ 10 at its peak. Interestingly, among the three lower redshift fields, the [O III]/[O II] line flux ratios as a function of spatial distance from the QSO exhibit different profiles. This difference confirms that significant variations in the underlying physical conditions, such as density, metallicity, and local ionizing radiation intensities, are present both within individual nebulae and between fields. However, quantifying the impact on the VSF measurements will require higher signal-to-noise data.

5.5 On the detection rate of QSO nebulae and its implications for turbulence studies

While the four QSO nebulae studied here exhibit a range of VSF slopes, a remaining question is how the results from this sample bear on quasar host halos as a whole. A fundamental limitation of the VSF measurements is the detectability of the diffuse gas, which is a combined result of instrument sensitivity and the physical conditions of the gas. Using the CUBS sample of 15 UV-bright QSOs (Chen et al. 2020), the detection rate of extended optical QSO nebulae (i.e. $\gtrsim 30$ kpc above the surface brightness level of $\sim 10^{-18}$ erg s^{-1} cm^{-2} arcsec^{-2}) at $z \lesssim 1.5$ is ≈ 25 per cent.[2] While a more comprehensive search of the MUSE data archive is needed to better quantify the detection rate of extended optical nebulae around QSOs, the ≈ 25 per cent detection rate from the CUBS programme most likely represents a conservative lower limit to the rate of incidence of extended nebulae around luminous QSOs. It remains to be determined as to whether deeper observations will both increase the detection rate of extended nebulae and uncover missing light at larger distances and lower flux levels.

With the current small sample size, no clear correlation is found between global QSO properties (e.g. luminosity, radio-loudness, number of group member galaxies), and the presence (or lack thereof) of extended optical nebulae. The current detection rate of extended nebulae around low-redshift QSOs is in stark contrast with the 100 per cent detection rate of extended Ly α nebulae around QSOs at $z \approx 3$, and could be a result of the possible redshift evolution of the cool ($\sim 10^4$ K) gas content at different epochs (e.g. Borisova et al. 2016; Arrigoni Battaia et al. 2019). However, a statistical sample of sources observed both in Ly α and non-resonant lines over cosmic time has yet to be established for a rigorous investigation of the apparent discrepancy in the incidence of extended nebulae between QSOs at low and high redshifts.

---

[2]Two of the four fields are presented in this study (i.e. J0454−6116 and J2135−5316), and two are not considered here due to their smaller sizes.
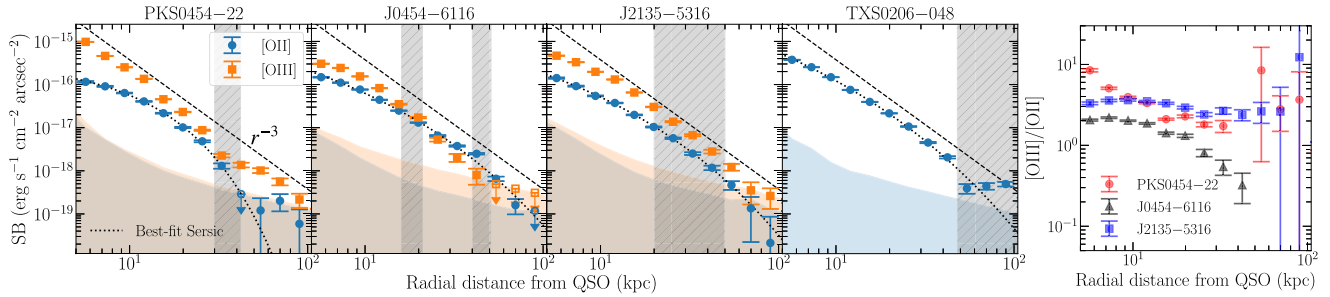
Figure 6. Surface brightness profiles of the four fields, and the corresponding [O III]/[O II] line flux ratios for the three lower redshift fields. The surface brightness profiles are circularly averaged within annuli at different distances from the QSOs. For the first three fields, vertical shaded regions indicate radii with relatively strong flux contributions from areas that are eliminated from the VSF measurements (see Section 3.5). For TXS0206−048, the vertical shaded region indicates the radii of the stream-like structures away from the main nebula (see Fig. 1). Blue and orange shaded regions at the bottom of each panel show the 2σ limit of the [O II] and [O III] surface brightness level as a function of radius. Dotted curves show the best-fitting Sérsic profiles for the [O II] line, with half-light radius $R_e \approx [10, 10, 9, 6]$ kpc and Sérsic index $n \approx [1.1, 2.6, 2.5, 3.0]$ for the four fields from left to right. For the [O III] profiles, however, we cannot find a good fit with Sérsic, exponential, or cored isothermal profiles. Instead, we overplot a power-law with −3 slope in dashed lines for comparison, as it provides a good match to the [O III] profile in PKS0454−22, as well as the [O II] and [O III] profiles outside of the core (≈ 10 kpc) region in other fields. In the right-most panel, [O III]/[O II] line flux ratios are shown for the three lower redshift fields, and data points with only upper limits on [O II] or [O III] are not included.

Meanwhile, evidence suggests that these nebulae could have a diverse range of physical origins. In addition to different [O III]/[O II] ratios (see Section 5.4 and Fig. 6), the morphology and the kinematics of nebulae also provide important clues. For example, the 'Makani' nebula exhibits morphokinematics that strongly suggests supergalactic winds being a predominant driver of the line-emitting region (Rupke et al. 2019). For PKS0454−22, the morphokinematics of the nebula and the continuum sources in the immediate vicinity of the QSO have led Helton et al. (2021) to argue that the extended nebula mostly consists of striped ISM through interactions between gas-rich galaxies. A similar case is made for the nebula in PKS0405−123 in Johnson et al. (2018) and TXS0206−048 (Johnson et al. 2022). However, this scenario of ISM stripping does not seem to be plausible for J0454−6116 and J2135−5316 studied here. For J2135−5316, only two group member galaxies (both far away from the location of the nebula) are found in the QSO field with the current data set (see Table 1). Similarly for the J0454−6116 field, although two continuum sources are found near the QSO, their velocities are inconsistent with the rest of the nebula and are likely not in a coherent dynamical system with the line-emitting gas (see Section 3.5). No additional companion continuum sources are found in this field that overlap with the nebula footprint. Interestingly, both J0454−6116 and J2135−5316 exhibit a relatively flat VSF. Future studies based on a larger sample are needed to investigate the respective roles of supergalactic winds and galactic environments in driving the turbulence of the CGM.

5.6 Limitations and caveats

A primary limitation of the current study is the relatively small dynamic range of length scales available for the VSF measurements. Specifically, the smallest scale accessible is limited by the FWHM of the effective PSF, which is a combination of the seeing disc in ground-based observations and the smoothing kernel applied to the final combined cubes to increase the SNR in the data (see Section 3.1). The largest scale is dictated by the size of the nebulae over which robust line signals can be measured. When measuring the slope of the VSF, the dynamic range is further restricted to where a single power law can provide an adequate description (see Section 4.1). Uncertainties in the VSF have also led to ambiguities in drawing conclusions on the dynamical properties of the gas. Even for TXS0206−048, the range

of distance scales probed is less than a decade. One possible way to increase the dynamic range is to target nebulae at lower redshifts. For example, at the same physical size, a nebula at $z \approx 0.1$ will be approximately $5 \times$ larger in the apparent angular size than those at $z \approx 1$, enabling VSF measurements on smaller scales for a fixed seeing disk size. Alternatively, to improve the measurements for nebulae at high redshifts, it is necessary to reduce the size of effective PSF in the data. The infrared spectrograph, NIRSpec, onboard the *James Webb Space Telescope* (*JWST*) will deliver a PSF 10 times smaller than the natural seeing disk on the ground. Using the upgraded adaptive optics assisted Narrow-Field-Mode provided by MUSE will also offer additional spatial resolving power for probing the energy power spectrum on scales as small as ∼1 kpc, but will require long exposures to reach sufficient SNR.

An improved spatial resolution also helps to reduce systematic uncertainties in the two-dimensional VSF measurements due to blending of distinct structures between adjacent sightlines. In analysing the [O II] $\lambda\lambda$ 3727, 3729 emission lines in all four fields, there is clear evidence for large density variations across individual nebulae based on the doublet ratio. If a large density contrast exists on scales smaller than the spatial resolution kernel, then blending would also suppress the power on small scales. Despite these caveats, it is interesting to see that the VSF measurements of three out of four nebulae in this study display a non-zero slope, indicating a clear scale-dependent power in the velocity structures.

6 CONCLUSION

In this study, we present measurements of the velocity structure functions for four optical nebulae detected in the vicinities of UV-luminous QSOs at $z \approx 0.5$–1.1. Using wide-field integral field spectroscopic data obtained from VLT/MUSE, we measure spatially resolved kinematics using the [O II] $\lambda\lambda$ 3727, 3729 and [O III] λ 5008 emission lines, and construct VSFs based on these velocity maps. Out of the four field, one field (i.e. TXS0206−048 with the largest nebula area and the highest SNR in the VSF measurement) exhibits a second-order VSF consistent with Kolmogorov, suggesting that the gas flows are isotropic and subsonic. We estimate a turbulent energy cascade rate of $\epsilon \approx 0.2$ cm^2 s^{-3}. The remaining three fields show a range of VSF slopes, while all being flatter than the Kolmogorov slope. Possible interpretations of the range of VSF slopes across the

four fields include the presence of a dynamically important magnetic field, turbulent energy injection at multiple spatial scales, a time-dependent evolution of the turbulent motions in the nebulae, and the impact from the diverse range of galactic environment associated with different fields. Alternatively, the apparent flat slopes in the VSFs may simply be due to a lack of dynamic range in the pair separations for probing the inertial range, which can be directly tested with high spatial resolution IFS data to extend the VSF measurements to smaller scales.

We develop the methodology to explicitly account for the spatial correlation in the data due to atmospheric seeing and smoothing. We also investigate possible contributions to the VSF measurements from a unidirectional velocity gradient, and large-scale radial or tangential rotational flows. These methods can be applied in future studies to obtain more robust VSF measurements. Our results improve upon traditional line width studies for inferring turbulent velocity fields in diffuse gas and provide a robust description of the energy power spectrum of the velocity field. The findings of this study can be compared with high-resolution numerical simulations to further our understanding of the driving and development of turbulence in the CGM, and the impact of quasar feedback on the CGM dynamics specifically in the case of quasar nebulae.

DATA AVAILABILITY

The data used in this article are available for download through the ESO Science Archive Facility.

REFERENCES

Anglés-Alcázar D., Faucher-Giguère C.-A., Kereš D., Hopkins P. F., Quataert E., Murray N., 2017, MNRAS, 470, 4698

Anorve-Zeferino G. A., 2019, MNRAS, 483, 704
Arrigoni Battaia F., Hennawi J. F., Prochaska J. X., Oñorbe J., Farina E. P., Cantalupo S., Lusso E., 2019, MNRAS, 482, 3162
Arthur S. J., Medina S. N. X., Henney W. J., 2016, MNRAS, 463, 2864
Astropy Collaboration, 2013, A&A, 558, A33
Bacon R. et al., 2010, Proc. SPIE, 7735, 773508
Bacon R., Piqueras L., Conseil S., Richard J., Shepherd M., 2016, MPDAF: MUSE Python Data Analysis Framework
Bacon R. et al., 2017, A&A, 608, A1
Benzi R., Ciliberto S., Tripiccione R., Baudet C., Massaioli F., Succi S., 1993, Phys. Rev. E, 48, R29
Boldyrev S., 2002, ApJ, 569, 841
Boldyrev S., 2006, Phys. Rev. Lett., 96, 115002
Borisova E. et al., 2016, ApJ, 831, 39
Brandenburg A., Lazarian A., 2013, Space Sci. Rev., 178, 163
Burkhart B., 2021, PASP, 133, 102001
Chen M. C., Chen H.-W., Gronke M., Rauch M., Broadhurst T., 2021, MNRAS, 504, 2629
Chen H.-W., 2017, Outskirts of Distant Galaxies in Absorption, Vol. 434. 291
Chen H.-W. et al., 2020, MNRAS, 497, 498
Chira R. A., Ibáñez-Mejía J. C., Mac Low M. M., Henning T., 2019, A&A, 630, A97
Cooper T. J. et al., 2021, MNRAS, 508, 4359
Fabian A. C., 2012, ARA&A, 50, 455
Federrath C., 2013, MNRAS, 436, 1245
Fielding D. B., Ostriker E. C., Bryan G. L., Jermyn A. S., 2020, ApJ, 894, L24
Foreman-Mackey D., Hogg D. W., Lang D., Goodman J., 2013, PASP, 125, 306
Frisch U., 1995, Turbulence. The legacy of A.N. Kolmogorov. Cambridge University Press, Cambridge, p. 72
Gaspari M. et al., 2018, ApJ, 854, 167
Grete P., O'Shea B. W., Beckwith K., 2021, ApJ, 909, 148
Gronke M., Oh S. P., Ji S., Norman C., 2022, MNRAS, 511, 859
Ha T., Li Y., Xu S., Kounkel M., Li H., 2021, ApJ, 907, L40
Ha T., Li Y., Kounkel M., Xu S., Li H., Zheng Y., 2022, ApJ, 934, 7
Haffert S. Y., Bohn A. J., de Boer J., Snellen I. A. G., Brinchmann J., Girard J. H., Keller C. U., Bacon R., 2019, Nature Astronomy, 3, 749
Helton J. M., Johnson S. D., Greene J. E., Chen H.-W., 2021, MNRAS, 505, 5497
Hu Y., Federrath C., Xu S., Mathew S. S., 2022, MNRAS, 513, 2100
Hunter J. D., 2007, Comput. Sci. Eng., 9, 90
Johnson S. D. et al., 2018, ApJ, 869, L1
Johnson S. D. et al., 2022, preprint (arXiv:2209.04245)
Kaplan S. A., Pikelner S. B., 1970, The Interstellar Medium. Harvard University Press, Cambridge
Kauffmann G. et al., 2003, MNRAS, 346, 1055
Kewley L. J., Dopita M. A., Sutherland R. S., Heisler C. A., Trevena J., 2001, ApJ, 556, 121
Kolmogorov A. N., 1941, Akademiia Nauk SSSR Doklady, 30, 301
Leclercq F. et al., 2017, A&A, 608, A8
Li Y. et al., 2020, ApJ, 889, L1
McNamara B. R., Nulsen P. E. J., 2007, ARA&A, 45, 117
Melnick J., Tenorio-Tagle G., Telles E., 2021, A&A, 649, A175
Mitchell P. D., Schaye J., 2022, MNRAS, 511, 2948
Mohapatra R., Jetti M., Sharma P., Federrath C., 2022, MNRAS, 510, 2327
Muzahid S. et al., 2020, MNRAS, 496, 1013
O'dell C. R., Castaneda H. O., 1987, ApJ, 317, 686
Oliphant T. E., 2015, Guide to NumPy, 2nd edn. CreateSpace Independent Publishing Platform, USA
Ossenkopf V., Mac Low M. M., 2002, A&A, 390, 307
Padoan P., Pan L., Haugbølle T., Nordlund Å., 2016, ApJ, 822, 11
Pan L., Scannapieco E., 2010, ApJ, 721, 1765
Pan L., Scannapieco E., 2011, Phys. Rev. E, 83, 045302
Patrício V. et al., 2016, MNRAS, 456, 4191
Péroux C. et al., 2019, MNRAS, 485, 1595
Planck Collaboration I, 2020, A&A, 641, A1
Price-Whelan A. M. et al., 2018, AJ, 156, 123

[3] https://ui.adsabs.harvard.edu/classic-form

Rauch M., Sargent W. L. W., Womble D. S., Barlow T. A., 1996, ApJ, 467, L5

Rauch M., Sargent W. L. W., Barlow T. A., 2001, ApJ, 554, 823

Rudie G. C., Steidel C. C., Pettini M., Trainor R. F., Strom A. L., Hummels C. B., Reddy N. A., Shapley A. E., 2019, ApJ, 885, 61

Rupke D. S. N., Gültekin K., Veilleux S., 2017, ApJ, 850, 40

Rupke D. S. N. et al., 2019, Nature, 574, 643

Saad T., Cline D., Stoll R., Sutherland J. C., 2017, AIAAJ, 55, 327

Sanderson K. N., Prescott M. M. K., Christensen L., Fynbo J., Møller P., 2021, ApJ, 923, 252

Savage B. D., Lehner N., Wakker B. P., Sembach K. R., Tripp T. M., 2005, ApJ, 626, 776

Schawinski K., Koss M., Berney S., Sartori L. F., 2015, MNRAS, 451, 2517

Sersic J. L., 1968, Atlas de Galaxias Australes. Observatorio Astronomico, Cordoba, Argentina

Sharma S., 2017, ARA&A, 55, 213

She Z.-S., Leveque E., 1994, Phys. Rev. Lett., 72, 336

Shen Y., 2021, ApJ, 921, 70

Steidel C. C., Bogosavljević M., Shapley A. E., Kollmeier J. A., Reddy N. A., Erb D. K., Pettini M., 2011, ApJ, 736, 160

Sun A.-L., Greene J. E., Zakamska N. L., 2017, ApJ, 835, 222

Tumlinson J., Peeples M. S., Werk J. K., 2017, ARA&A, 55, 389

van de Voort F., 2017, in Fox A., Davé R., eds, Astrophysics and Space Science Library, Vol. 430, Gas Accretion onto Galaxies. Springer International Publishing AG, Cham, p. 301

Virtanen P. et al., 2020, Nature Methods, 17, 261

von Hoerner S., 1951, ZAp, 30, 17

Weilbacher P. M. et al., 2020, A&A, 641, A28

Wen Z., O'dell C. R., 1993, ApJ, 409, 262

Wisotzki L. et al., 2016, A&A, 587, A98

Xie C., Haffert S. Y., de Boer J., Kenworthy M. A., Brinchmann J., Girard J., Snellen I. A. G., Keller C. U., 2020, A&A, 644, A149

Xu S., 2020, MNRAS, 492, 1044

Zahedy F. S., Chen H.-W., Johnson S. D., Pierce R. M., Rauch M., Huang Y.-H., Weiner B. J., Gauthier J.-R., 2019, MNRAS, 484, 2257

Zahedy F. S. et al., 2021, MNRAS, 506, 877

Zhang C., Zhuravleva I., Gendron-Marsolais M.-L., Churazov E., Schekochihin A. A., Forman W. R., 2022, MNRAS, 517, 616

Zhuravleva I. et al., 2014, Nature, 515, 85

ZuHone J. A., Markevitch M., Zhuravleva I., 2016, ApJ, 817, 110

APPENDIX A: SOME EXTRA MATERIAL

Here we present the VSFs measurements for PKS0454−22, J0454−6116, and J2135−5316. The results are discussed in Sections 4.4 and 5.
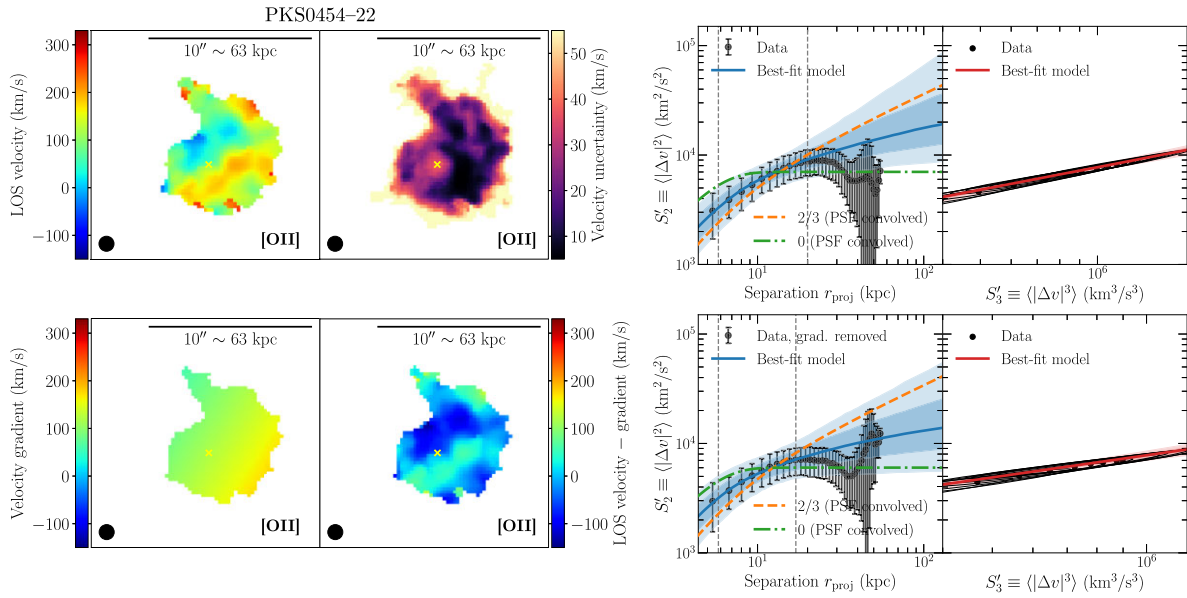

Figure A1. Same as Figs 3 and 4 in the main text, but for the field of PKS0454−22 using the [O II] λλ 3727, 3729 emission line. Here, a flat VSF (with a slope of 0) is also shown by the dot–dashed green line for comparison.
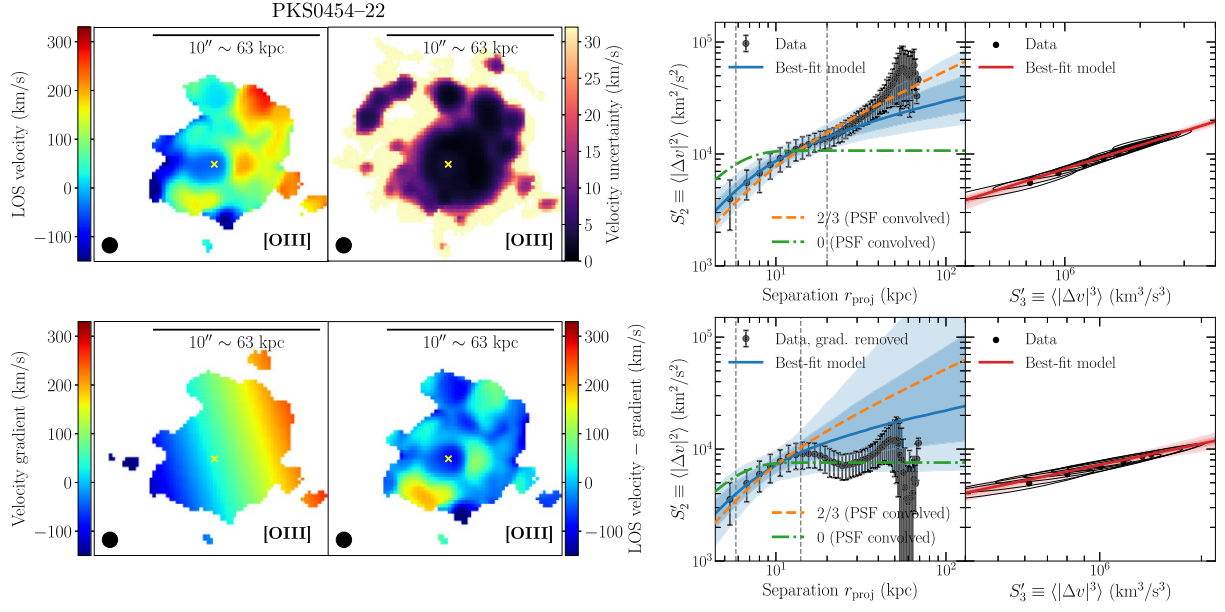
Figure A2. Same as Figs 3 and 4 in the main text, but for the field of PKS0454−22 using the [O III] λ 5008 emission line. Here, a flat VSF (with a slope of 0) is also shown by the dot–dashed green line for comparison.
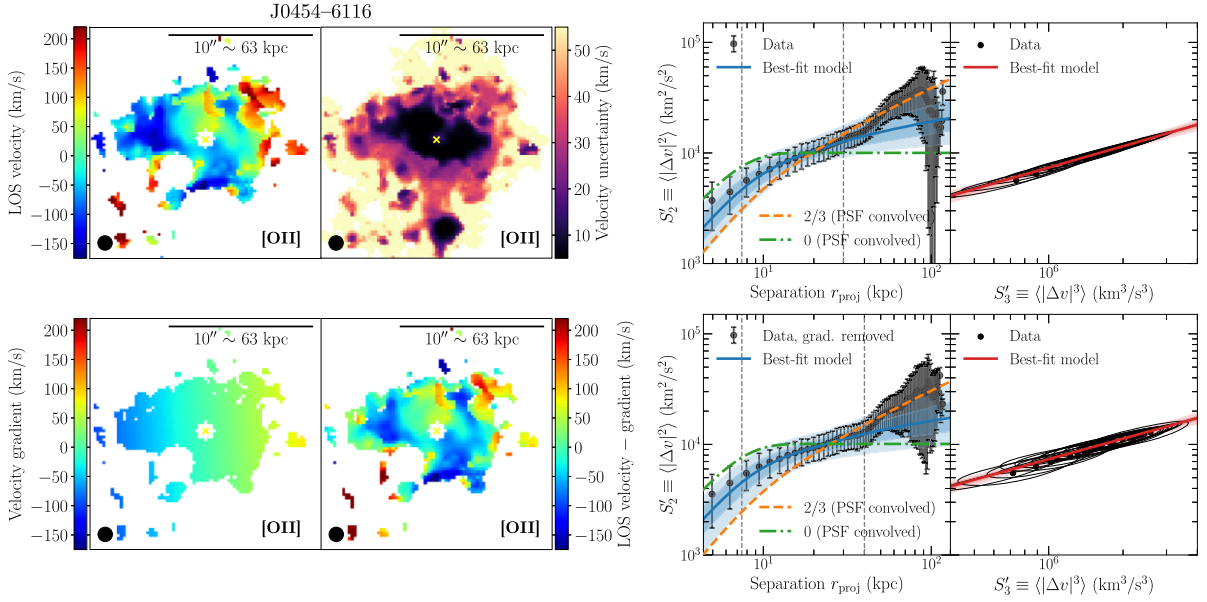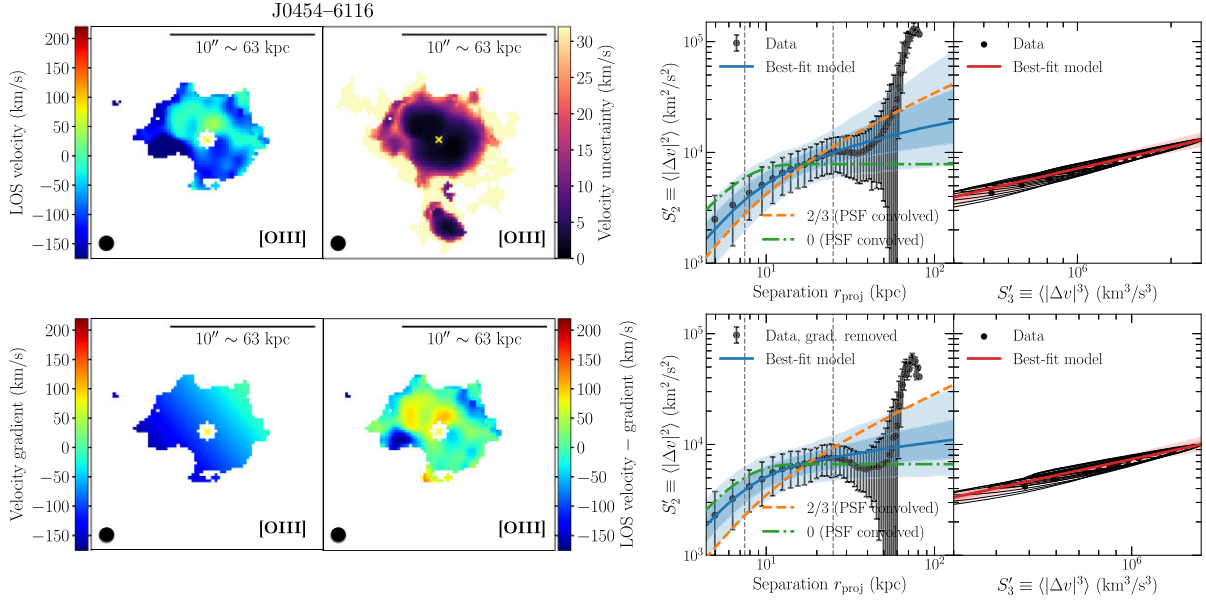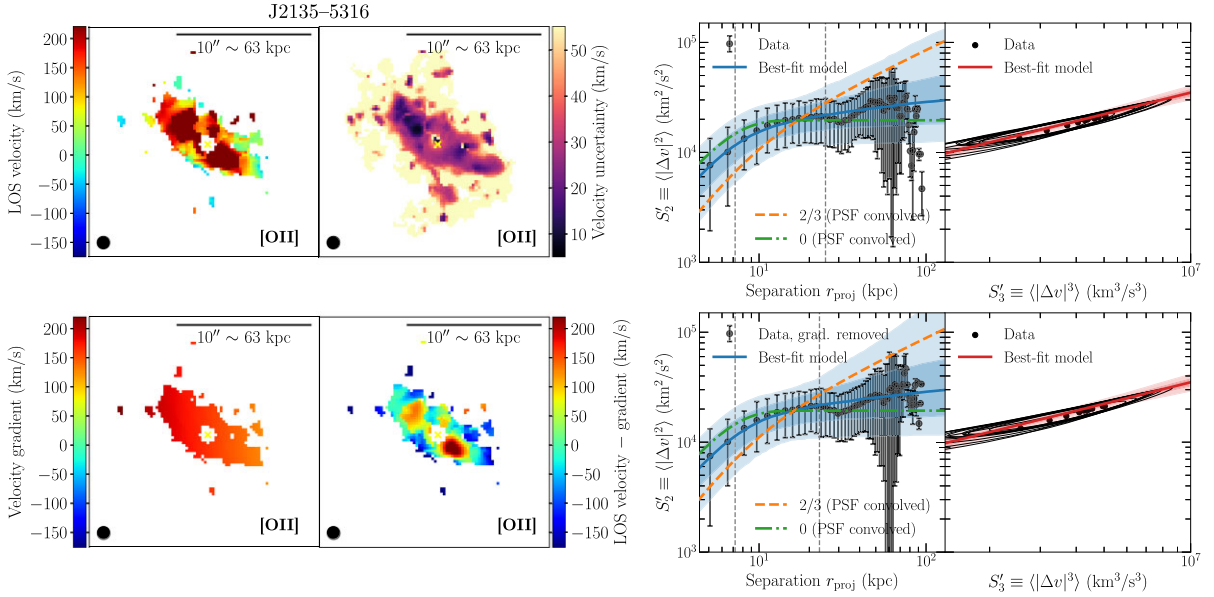

Figure A3. Same as Figs 3 and 4 in the main text, but for the field of J0454−6116 using the [O II] λλ 3727, 3729 emission line. Here, a flat VSF (with a slope of 0) is also shown by the dot–dashed green line for comparison.
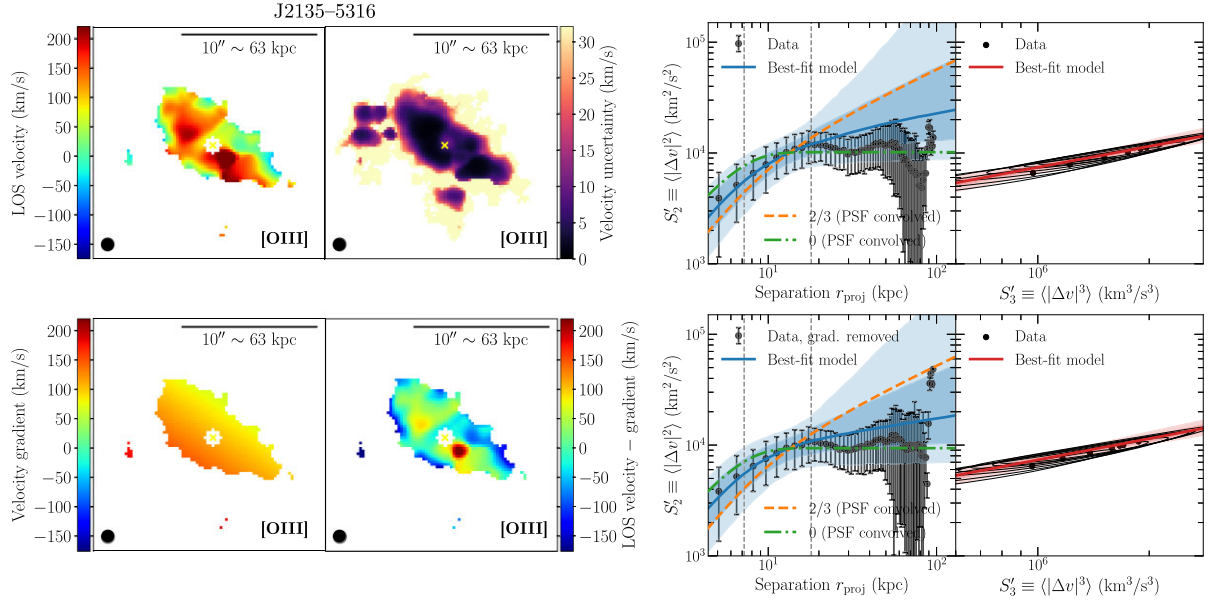
Figure A4. Same as Figs 3 and 4 in the main text, but for the field of J0454−6116 using the [O III] λ 5008 emission line. Here a flat VSF (with a slope of 0) is also shown by the dot–dashed green line for comparison.

Figure A5. Same as Figs 3 and 4 in the main text, but for the field of J2135−5316 using the [O II] λλ 3727, 3729 emission line. Here, a flat VSF (with a slope of 0) is also shown by the dot–dashed green line for comparison.

Figure A6. Same as Figs 3 and 4 in the main text, but for the field of J2135−5316 using the [O III] λ 5008 emission line. Here, a flat VSF (with a slope of 0) is also shown by the dot–dashed green line for comparison.
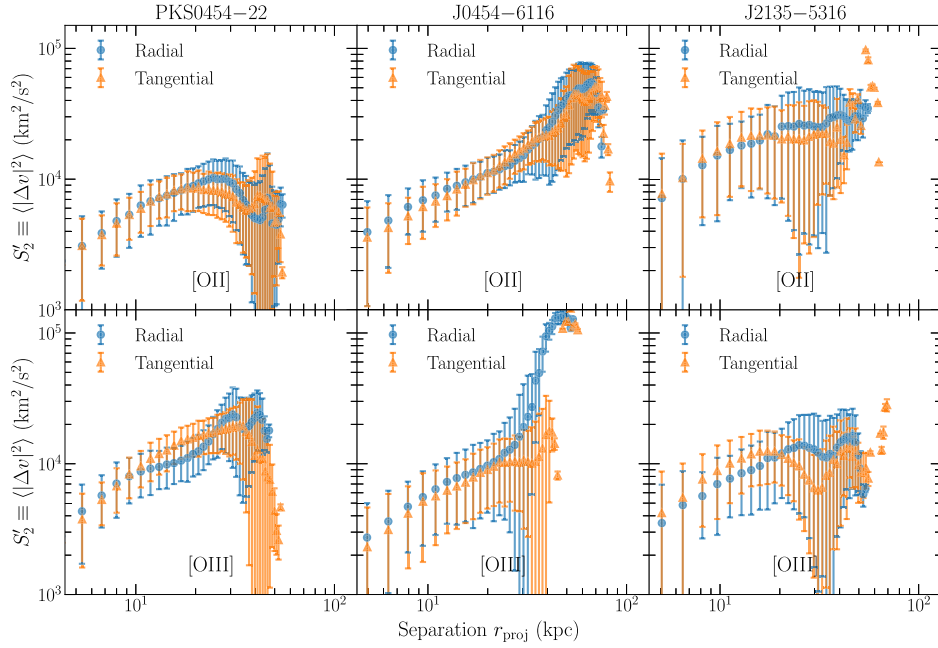

Figure A7. Same as the right panel of Fig. 5, but for the fields of PKS0454−22, J0454−6116, and J2135−5316, including results based on both [O II] λλ 3727, 3729 and [O III] λ 5008 emission lines.
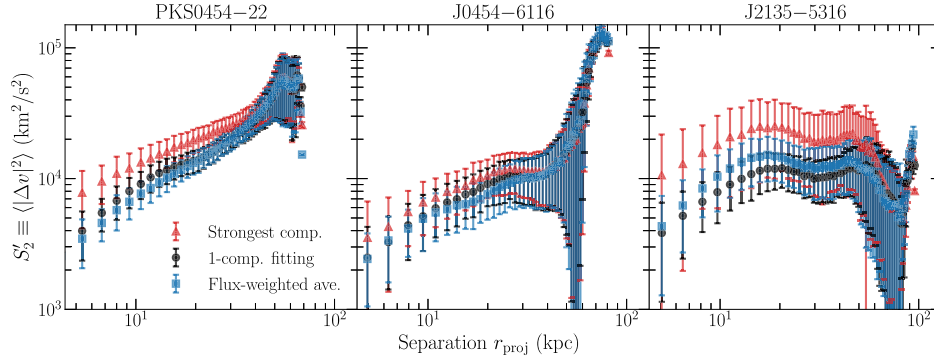
Figure A8. Comparison of the VSF measurement under three different scenarios where we assign to the multicomponent spaxels (1) the velocity of the components with the most flux in each spaxel (i.e. the strongest component), (2) the velocity obtained by a one-component fit (i.e. ignoring the presence of multiple components), and (3) the flux-weighted mean velocity among all components.
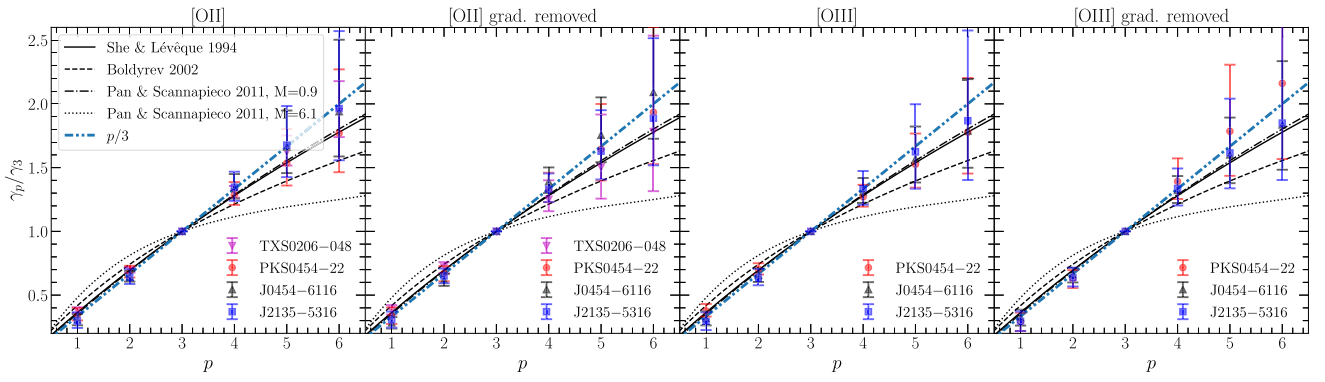

Figure A9. Estimated power-law slopes γ_p of S_p with p ranging from $p = 1$ to $p = 6$ for all four nebulae. Different γ_p's are normalized to γ_3 for measurements based on [O II] $\lambda\lambda$ 3727, 3729 and [O III] λ 5008 velocity maps as well as their corresponding velocity residual maps after removing a unidirectional coherent gradient (see Section 4.2). Data points represent the median values obtained with the 1000 modified bootstrap samples (see Section 3.5), and the error bars indicate the 16th and 84th quantiles. Note that the ratio γ_p/γ_3 only equals to γ_p if $\gamma_3 = 1$. The solid curve shows the expected γ_p/γ_3 ratio for subsonic Kolmogorov turbulence with the intermittency correction presented in She & Leveque (1994). The expected γ_p/γ_3 ratio for supersonic magnetohydrodynamic turbulence presented in Boldyrev (2002) is shown by the dashed curve. The dash–dotted (dotted) curve indicates the γ_p/γ_3 ratio derived from numerical hydrodynamic turbulent simulations for Mach number $M = 0.9$ ($M = 6.1$) as presented in Pan & Scannapieco (2011). Finally, the blue loosely dash–dotted curve shows the expected γ_p/γ_3 ratio for Kolmogorov turbulence without the intermittency correction, which simply scales as $p/3$. See Section 5.3 for further discussions.

This paper has been typeset from a TEX/LATEX file prepared by the author.